VLASOV SIMULATION OF CURRENT-DRIVEN INSTABILITIES RELEVANT TO HIGH-CURRENT HOLLOW CATHODE PLUMES

A Thesis

by

CAMERON JAMES TREECE

Submitted to the Office of Graduate and Professional Studies of
Texas A&M University
in partial fulfillment of the requirements for the degree of

MASTER OF SCIENCE

Chair of Committee,	Kentaro Hara
Committee Members,	Alexei Poludnenko
	David Staack
Head of Department,	Rodney Bowersox

August 2019

Major Subject: Aerospace Engineering

ABSTRACT

Understanding the sputtering of cathode surfaces is of high interest to the EP community, since hollow cathodes can be one of the main lifetime limiting components of Hall thrusters and ion engines. Current-driven instabilities in the plumes of hollow cathodes are a leading candidate for the mechanism behind the generation of high energy ions that erode hollow cathode surfaces and result in an anomalous momentum loss of the electron current. A 1D Vlasov simulation is used to study the ion kinetics and time evolution of bulk plasma properties in the nonlinear saturation regime of the current-carrying instability. The simulations are carried out over a range of initial electron Mach numbers, $0.5 \leq M_0 \leq 2.5$, where the electron Mach number is defined as the ratio of the relative drift velocity between electrons and ions to the electron thermal velocity. Time evolution of the bulk plasma properties show significant plasma heating and current dissipation, resulting in a decrease in the steady-state electron Mach number as the initial condition M_0 increases. This steady state value is what is measured in experiments and illustrates the nonlinear time dependence of the instability and, due to its rapid growth, the difficulty in understanding its true nature from experimental data. High energy ions are generated due to large amplitude ion acoustic waves of large phase velocities. A significant population of backstreaming high energy ions is observed when the initial electron Mach number is greater than or equal to 1.3, indicating a transition to the Buneman instability, where nonlinear kinetic effects are dominant. The population and velocity ranges of the high energy ions are extracted and used to calculate sputtering rates, which are compared to calculations using the non-Maxwellian distributions for ions obtained from the simulation and Maxwellian ion distributions of temperatures ranging from 0.5 eV to 4.0 eV. The very large ion temperatures required by the Maxwellian distributions to obtain the same level of sputtering as the kinetic model illustrate the necessity of self-consistent kinetic models in fluid simulations to capture the cathode erosion.

DEDICATION

To my mother and my father.

ACKNOWLEDGMENTS

I am very appreciative of my advisor, Dr. Kentaro Hara, for being so patient with and supporting of me during my graduate study. I am thankful for my friends and family for providing my life with a stabilizing foundation. I am forever grateful for my best friends, Jacob Roby, Bethany Babcock, and little Weasel, for always being there for me when I need them.

CONTRIBUTORS AND FUNDING SOURCES

Contributors

This work was supported by a thesis committee consisting of Professor Kentaro Hara and Professor Alexei Poludnenko of the Department of Aerospace Engineering and Professor David Staack of the Department of Mechanical Engineering. The author acknowledges collaboration with his advisor Professor Kentaro Hara throughout the course of this research and the Texas A&M High Performance Research Computing facility for providing their hardware and software.

All other work conducted for the thesis was completed by the student independently.

Funding Sources

This material is based upon work supported by the U.S. Department of Energy, Office of Science, Office of Fusion Energy Sciences under Award Number DE-SC0019045. Graduate study was supported by a grant by the Japan Aerospace Exploration Agency and the Department of Aerospace Engineering at Texas A&M University.

TABLE OF CONTENTS

Page

LIST OF FIGURES

FIGURE Page

1. INTRODUCTION

Hollow cathodes are a critical component for electric propulsion (EP) devices such as the ion engine and Hall thruster. In ion engines, there are typically two hollow cathodes: one is mounted internally within the discharge chamber and supplies the electrons that ionize the propellant gas, and another hollow cathode is mounted externally and supplies the electrons that neutralize the expelled ion beam. In Hall thrusters, one externally-mounted hollow cathode is used for both of these purposes, where some portion of the electrons enter the Hall thruster discharge channel to participate in ionization and the rest of the electrons participate in the neutralization of the ion beam. A schematic of a hollow cathode is shown in Figure 1.1. It consists of a heat-resistant tube surrounded by a heating element, and within the tube is placed an insert material that, at appropriate temperatures, emits electrons via thermionic emission. Inside the tube, neutral propellant gas is injected at the cathode and at the other end is an orificed plate that allows electrons to be extracted from the discharge. External to the orifice plate is the keeper electrode, which serves to maintain

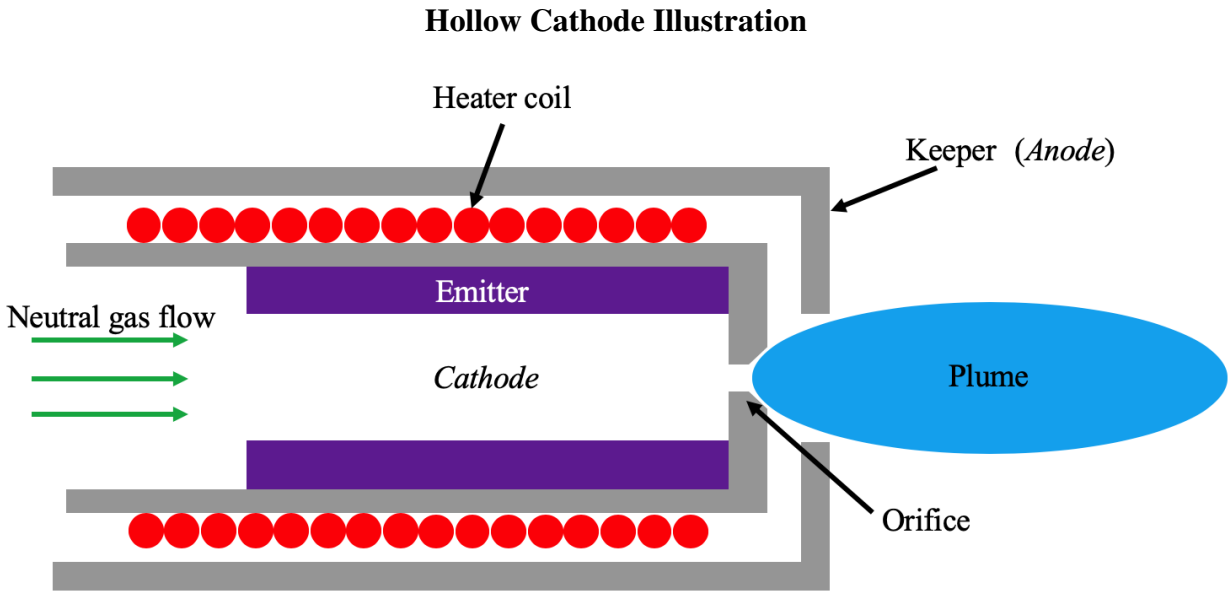

Figure 1.1: Illustration of a hollow cathode used for electric propulsion, including the emitter, orifice, and plume regions.

cathode operation and protect the orifice plate from bombardment by high energy ions. The keeper electrode is usually biased to a positive voltage to initiate cathode startup and reduce the energy of incident ions. The integrity of the keeper and orifice plate is critical to the lifetime of the hollow cathode.

The hollow cathode plasma can be divided into three distinct regions. First is the insert region, which consists of a high density, low temperature, low potential discharge plasma during steady state operation. Insert materials such as scandate, barium oxide (BaO), and tungsten have been successfully used in hollow cathodes [1]. Lanthanum-hexaboride (LaB_6) has more recently received more attention due to its low work function and resistance to poisoning and evaporation, leading to high emission current densities and long lifetime of the insert material [2]. During the hollow cathode startup process, the heating element is active to heat the insert such that thermionically emitted electrons can initiate the ionization process and ignite the discharge. Once the discharge temperature is high enough, the heating element is deactivated and thermionic emission is sustained through self-heating from the discharge plasma. The second region is the orifice, where the plasma is confined to a much smaller diameter and the current density is large. As the potential increases through the orifice, electrons are expelled from the insert region into the third region, the plume. Electrons accelerated in the plume expansion can cause streaming instabilities that may experience weak collisional damping, resulting in non-Maxwellian velocity distribution functions (VDFs) for both electrons and ions.

Two important physical phenomena in hollow cathodes include erosion and anomalous electron transport. Mikellides et al. appear to be the first to propose that current-driven instabilities leading to ion acoustic turbulence (IAT) result in an anomalous resistivity near the orifice region [3, 4], and later work by Jorns et al. appear to be the first to experimentally confirm the existence of IAT in the hollow cathode plume [5]. It has also been shown that anomalous electron transport due to the growth and saturation of current-driven instabilities must be taken into account in numerical models to obtain good agreement with experimental data [3, 4]. The other consequence of the kinetic instabilities leads to anomalously high erosion rate of hollow cathode components [6],

which may limit the lifetime of EP missions. One hypothesis for the cause of hollow cathode erosion is identified as high energy ions generated by large amplitude potential fluctuations in the cathode discharge due to ion acoustic and ionization instabilities [6, 7]. It has been shown that accounting for these fluctuations in a fluid model can produce erosion profiles in close agreement with those observed in experiments [8]. While the high energy ion population could be significantly less than the bulk ion population, it is these ions that are most likely to pose the greatest contribution to sputtering over long periods of time as they overcome the threshold energies of sputtering.

Extended Life Tests (ELT) from Goebel et al. [6] for the NASA Solar electric propulsion Technology Applications Readiness (NSTAR) and the Nuclear Electric Xenon Ion System (NEXIS) configuration ion thruster hollow cathodes show that the plasma potential 3 mm downstream of the keeper plate increases radially, and the potential fluctuations reach a maximum voltage amplitude at some radial distance ~ 0.8 cm relative to the cathode centerline. Goebel et al. also show images of the radial erosion profile of the keeper plate after an 8200 hour Life Demonstration Test (LDT), with the erosion being maximum some short radial distance from the centerline, consistent with the radial location of the maximum potential amplitude fluctuations. It is expected that collisions in the higher density region at the cathode centerline will result in increased damping of the instability. Due to the decreasing radial plasma density profile resulting from the plume expansion, it is possible that the generation of high energy ions from the instability reaches a maximum some radial distance from the cathode centerline, and that these high energy ions then lead to the observed radial profile of orifice plate erosion.

Classical collisions can be up to 3 orders of magnitude less frequent than in the insert plasma and up to 2 orders of magnitude less frequent than proposed anomalous scattering mechanisms [8]. Ong and Yu show that weak classical collisions can reduce the effectiveness of Landau damping by disrupting the resonance, and that weak classical collisions may reduce the threshold velocity needed for instability [9]. In contrast, Epperlein et al. show that although electron-ion collisions can inhibit Landau damping, collisional damping is still the dominant effect [10]. While classical collisions are necessary physics for fully predictive hollow cathode simulations, the absence of

collisions used here allow for a simplified environment to study the the relationship between the initial conditions, saturation, and the generation of high energy ions resulting from the instability in the plume. Also relevant to the anomalous physics in the plume of high current hollow cathodes are the magnetic field (applied from a thruster and self-induced due to high current density) and multi-dimensional effects. The magnetic field confines the plasma in the region downstream of the orifice, increasing the plasma density along the centerline [11, 12, 13], which would be expected to dampen the instability along the centerline but may enhance growth in the radial direction. Two-dimensional (2D) plasma wave propagation is complex and involves wavefront bowing and sideloss [14], a mechanism for the detrapping of particles from large amplitude waves, or steep potential gradients that in 1D would not otherwise occur.

Linear instabilities and nonlinear saturation are well studied using kinetic simulations for various types of beam-plasma phenomena [15, 16, 17, 18, 19, 20]. Current-driven instabilities have previously been investigated but used artificial mass ratios, e.g. $m_i/m_e = 4$, and a small velocity domain [21, 22]. While anomalous electron transport models have shown promising success in hollow cathode plasmas [3, 13, 23], it is necessary to account for nonlinear ion dynamics in the kinetic evolution of the ion velocity distribution function.

Computer simulations have enabled the advancement of understanding of the hollow cathode physics. Kinetic particle methods such as particle-in-cell (PIC) employ on the order of dozens of computational particles per cell and resolving the ion kinetics over the statistical noise inherent to PIC requires a much larger number of computational particles by many orders of magnitude. Modeling electrons using a kinetic method is prohibitively expensive, particularly when the electron density varies a few orders of magnitude. The numerical method most often used for hollow cathode plasmas is a fluid model, which is computationally more efficient than PIC and grid-based direct kinetic (DK) methods [24]. Several fluid models have been developed to account for the kinetic effects due to the current-driven instabilities by using anomalous electron transport coefficients. Mikellides et al. developed a plasma fluid model that accounts for the anomalous electron momentum exchange frequency using the wave energy [3, 7]. Further development has been made

to propose a wave growth model employing a transport equation of the plasma wave energy based on quasilinear theory and nonlinear saturation [25, 26]. The linear growth rate of the instabilities is evaluated from local plasma properties such as the electron Mach number, $M = u_e/v_{th,e}$, where u_e is the electron bulk velocity and $v_{th,e}$ is the electron thermal velocity. It was also discussed that ion heating plays an important role since ion Landau damping of the current-driven instabilities depends on the electron-to-ion temperature ratio, T_e/T_i, where T_e is the electron temperature and T_i is the ion temperature [13]. Sary et al. used a similar wave growth model that captures time dependent anomalous electron transport, which seemed to cause ionization oscillations [11, 12]. Kubota et al. developed a hybrid-PIC simulation using a Monte Carlo technique to model high energy ions [27].

In Chapter 2, kinetic theory leading to the Vlasov formulation of collisionless plasmas and the basic theories of the ion acoustic instabilities are reviewed. In Chapter 3, the grid-based DK method used for the Vlasov-Poisson simulation is discussed. In Chapter 4 we discuss the kinetic effects of the current-driven instabilities as a function of initial electron Mach number. We show the linear growth and saturation phases of the instability and the time evolution of bulk plasma properties, including anomalous resistivity and electron and ion VDFs, which can be used as input conditions for hollow cathode fluid simulations. A model that describes generation of high energy ions due to trapping in the plasma waves is provided. We present dispersion diagrams for various electron Mach numbers that show clearly the nature of the plasma waves during saturation, including the maximum phase velocity of the waves, and show the dependence of the maximum phase velocity on initial electron Mach number. We present ion energy distribution functions (EDFs) and discuss how the maximum ion energies relate to the maximum phase velocities of the plasma waves. Sputtering rate calculations show a significant difference between the non-Maxwellian ion VDFs obtained from the DK simulation and Maxwellian distributions with various ion temperatures. Finally, in Chapter 5 we present conclusions and discuss ideas for future work to develop predictive models the anomalous resistivity, high energy ion generation and hollow cathode erosion.

2. PLASMA THEORY

2.1 Modeling Plasmas

A plasma is a gas where there exists some considerable degree of net-charge carriers that (i) is quasineutral and (ii) exhibits collective behavior. As a result, plasmas behave very differently than typical gases and are referred to by some as a separate state of matter. Plasma is the most abundant state of matter in the universe and is characterized by a wide range of densities and temperatures. Like any gas, the proper choice for modeling plasma depends on the physics involved within the density and temperature regime. One of the most important parameters to consider for modeling plasma is the Knudsen number.

2.1.1 Mean Free Path and Knudsen Number

Consider a collection of particles in random motion. Two or more particles will interact if they come within sufficient proximity to one another. These mutual particle interactions can be treated as collisions, and vary in interaction distance and scattering properties based on the particle species and energy state. The mean distance that a particle travels through free space before encountering a collision is called the mean free path, λ, which is proportional to the number density, n, and collision cross-section, σ,

$$\lambda \propto \frac{1}{n\sigma}.$$

The collisionality will depend on the mean free path and a physical length scale relevant to the problem. For example, the length scale in cosmological plasmas may be many millions of kilometers, while the length scale in a hollow cathode will be on the order or millimeters or centimeters. A plasma with a mean free path of 1 m will be considered collisionless if viewed within the context of a typical electric propulsion device, but it will be considered highly collisional if viewed within the context of the interstellar medium. The Knudsen number, Kn, is a quantitative measure of this collisionality, defined as the ratio of the mean free path to the relevant physical length scale, L,

$$\mathrm{Kn} = \frac{\lambda}{L}.$$

For $\mathrm{Kn} \ll 1$, the plasma can be modeled as a continuum with well defined volume-averaged or macroscopic properties. For $\mathrm{Kn} \to \infty$, the flow is in the free-molecular regime and a kinetic description is required. Between these extremes is a transition regime where effects of thermal non-equilibrium are significant but collisions still play an important role.

2.1.2 The Boltzmann Equation

The Boltzmann equation is one of a hierarchy of equations along the path of model reduction from a microscopic to a macroscopic description. The discussion in this section will follow that given in the book by Stewart Harris, *An Introduction to the Theory of the Boltzmann Equation* [28]. The state of a system of N particles can be described by the generalized position $\vec{q}_i$ and momentum $\vec{p}_i$ of each particle, which together are called canonical coordinates. The equations of motion for this system of N particles can be calculated from the Hamiltonian of the system,

$$\dot{\vec{q}}_i = \frac{\partial H}{\partial \vec{p}_i} \tag{2.1}$$

$$\dot{\vec{p}}_i = -\frac{\partial H}{\partial \vec{q}_i} \tag{2.2}$$

$$i = 1, 2, 3, \ \ldots, N.$$

Equations (2.1) and (2.2) represent the time-rate of change of the canonical coordinates (trajectories) in a $6N$-dimensional space called the phase space. The system is completely deterministic in that if we have knowledge of the forces on each particle i and some instantaneous condition for all $\vec{q}_i$ and $\vec{p}_i$ at some time t, then the microscopic state of the system at any future or past time can be computed. The state of the system of N particles is given by a single point in this $6N$-dimensional phase space.

A basic postulate of statistical mechanics which applies both to systems in equilibrium and nonequilibrium is that all intensive macroscopic properties of a system, G, can be described in

terms of the microscopic states of that system, so $G = G\left(\{\vec{q}(t)\}, \{\vec{p}(t)\}\right)$. Any observed intensive macroscopic property, G_{obs}, of the system is realistically going to be obtained by some measurement that must occur over some finite time interval τ. G_{obs} could be the measured temperature, pressure, or density, for example. Thus G_{obs} can be calculated from a time-average of the instantaneous value $G\left(\{\vec{q}(t)\}, \{\vec{p}(t)\}\right)$,

$$G_{obs} = \bar{G} = \frac{1}{\tau}\int_{t_0}^{t_0+\tau} G\left(\{\vec{q}(t)\}, \{\vec{p}(t)\}\right) dt, \tag{2.3}$$

where t_0 is the time at which the measurement begins, the state of the system is given by equations (2.1) and (2.2), and the overbar denotes the time average. Calculation of G_{obs} is impossible due to large number of degrees of freedom (there are $6N$ equations to solve, where N could be on the order of Avogadro's number N_A).

Let η represent the number of microstates that comprise a macroscopic system. Josiah Gibbs formulated the method of ensembles, where the macroscopic system of N particles is divided into a large number of η microscopic systems, referred to as an ensemble. Just like the macroscopic system was represented by a point in the $6N$-dimensional phase space, so too are each of the η microscopic systems represented by a point in the phase space. However, for the microscopic systems, these points are not specified. Rather, we visualize these microscopic systems, each with its own state, as collectively belonging to a distribution of states. For $\eta \to \infty$, the phase space volume elements $d\vec{q}_i d\vec{p}_i$ become infinitely fine grained, and this distribution of states can be represented by a continuous density function, which can be normalized such that it is defined to be a probability density distribution, $F_N = F_N\left(\{\vec{q}\}, \{\vec{p}\}, t\right)$. The fraction, Q, of the η microscopic systems or states that can be found within a phase space volume element $d\vec{q}_i d\vec{p}_i$ about the point $(\{\vec{q}\}, \{\vec{p}\})$ at time t can be found by integrating F_N along each of the $6N$ dimensions:

$$Q = F_N\left(\{\vec{q}\}, \{\vec{p}\}, t\right) \prod_{i=1}^{N} d\vec{q}_i d\vec{p}_i. \tag{2.4}$$

Another basic postulate of statistical mechanics is the ergodic statement, which says that given

a sufficient period of time, all microstates accessible by the system are equally probable. This means that taking an ensemble average of a macroscopic quantity, $\langle G\left(\{\vec{q}\},\{\vec{p}\},t\right)\rangle$, is equivalent to taking the time average,

$$\langle G(t)\rangle = \bar{G}(t).$$

Thus, rather than calculating observed macroscopic properties by time averaging via equation (2.3), we can instead take an ensemble average, given by

$$\langle G(t)\rangle = \int G\left(\{\vec{q}\},\{\vec{p}\},t\right) F_N\left(\{\vec{q}\},\{\vec{p}\},t\right) \prod_{i=1}^{N} d\vec{q}_i d\vec{p}_i. \tag{2.5}$$

We would like to know how the probability distribution function F_N evolves in time due to the natural motion of the η microstates in phase space, determined by equations (2.1) and (2.2). The infinitesimal change, dF_N, of the value of $F_N\left(\{\vec{q}\},\{\vec{p}\},t\right)$ results from infinitesimal changes in the variables $\{\vec{q}\}$, $\{\vec{p}\}$, and t, which can be written as

$$dF_N = \frac{\partial F_N}{\partial t}dt + \sum_{i=1}^{N} \frac{\partial F_N}{\partial \vec{q}_i}\cdot d\vec{q}_i + \sum_{i=1}^{N} \frac{\partial F_N}{\partial \vec{p}_i}\cdot d\vec{p}_i. \tag{2.6}$$

Using $d\vec{q}_i = \dot{\vec{q}}_i dt$, $d\vec{p}_i = \dot{\vec{p}}_i dt$, $\dot{\vec{q}}_i = \vec{p}_i/m$, and $\dot{\vec{p}}_i = \vec{F}_i$, we can rewrite equation (2.6),

$$\frac{dF_N}{dt} = \frac{\partial F_N}{\partial t} + \sum_{i=1}^{N}\left[\frac{\partial F_N}{\partial \vec{q}_i}\cdot\frac{\dot{\vec{p}}_i}{m} + \frac{\partial F_N}{\partial \vec{p}_i}\cdot\vec{F}_i\right]. \tag{2.7}$$

Liouville's theorem states that the probability distribution function F_N remains constant in time along the phase space trajectories,

$$\frac{dF_N}{dt} = 0.$$

Thus,

$$\frac{\partial F_N}{\partial t} + \sum_{i=1}^{N}\left[\frac{\partial F_N}{\partial \vec{q}_i}\cdot\dot{\vec{q}}_i + \frac{\partial F_N}{\partial \vec{p}_i}\cdot\dot{\vec{p}}_i\right] = 0. \tag{2.8}$$

This is Liouville's equation, and expresses an incompressible flow of the field $F_N\left(\{\vec{q}\},\{\vec{p}\},t\right)$ in

phase space. At this point, the problem still consists of $6N$ degrees of freedom and remains fully deterministic and reversible.

A dimensional contraction of equation (2.8) can be performed by introducing a set of reduced distribution functions with $R \leq N$ degrees of freedom, F_R, which are defined by integrating out the degrees of freedom of other particles,

$$F_R\left(\vec{q}_1,\ \ldots,\vec{q}_R,\vec{p}_1,\ \ldots,\vec{p}_R,t\right) = \int F_N\left(\{\vec{q}\},\{\vec{p}\},t\right) \prod_{i=R+1}^{N} d\vec{q}_i d\vec{p}_i. \tag{2.9}$$

We can express the forces $\vec{F}_i$ as the pair potentials between particles i and j, $\vec{\phi}_{ij}$, and the external fields as $\vec{\phi}_i^{ext}$,

$$\vec{F}_i = -\sum_{j\neq i} \frac{\partial \vec{\phi}_{ij}}{\partial \vec{q}_i} - \frac{\partial \vec{\phi}_i^{ext}}{\partial \vec{q}_i}. \tag{2.10}$$

Integrating F_N as shown in equation (2.9) and substituting the potentials for $\vec{F}_i$, a system of equations can be derived,

$$\begin{aligned} &\frac{\partial F_R}{\partial t} + \sum_{i=1}^{R} \frac{\vec{p}_i}{m}\frac{\partial F_R}{\partial \vec{q}_i} - \sum_{i=1}^{R}\left(\sum_{j\neq i}^{R} \frac{\partial \vec{\phi}_{ij}}{\partial \vec{q}_i} + \frac{\partial \vec{\phi}_i^{ext}}{\partial \vec{q}_i}\right)\frac{\partial F_R}{\partial \vec{p}_i} \\ &\qquad = (N-R)\sum_{i=1}^{R}\int \frac{\partial \vec{\phi}_{i\ R+1}}{\partial \vec{q}_i}\frac{\partial F_{R+1}}{\partial \vec{p}_i} d\vec{q}_{R+1} d\vec{p}_{R+1}. \end{aligned} \tag{2.11}$$

This is known as the Bogolyubov-Born-Green-Kirkwood-Yvon, or BBGKY, hierarchy of equations, named after Nikolay Bogolyubov, Max Born, Herbert Green, John Kirkwood, and Jacques Yvon. The degrees of freedom have been lowered from $6N$ to $6R$, but this system of equations is not closed. The BBGKY system is a hierarchy because the distribution function F_R is a function of the distribution function F_{R+1}; it is a coupled chain of equations. The time evolution of the distribution function F_R is governed by a Liouville-like equation with the inclusion of a correction term that represents the influence of the forces on F_R from the suppressed $(N-R)$ particles. In

particular, we are interested in the first two equations for the time-evolution of F_1 and F_2,

$$\frac{\partial F_1}{\partial t} + \frac{\vec{p_1}}{m}\frac{\partial F_1}{\partial \vec{q_1}} - \frac{\partial \vec{\phi}_1^{ext}}{\partial \vec{q_1}}\frac{\partial F_1}{\partial \vec{p_1}} = (N-1)\int \frac{\partial \vec{\phi}_{12}}{\partial \vec{q_1}}\frac{\partial F_2}{\partial \vec{p_1}}, \tag{2.12}$$

$$\begin{aligned}\frac{\partial F_2}{\partial t} + \frac{\vec{p_1}}{m}\frac{\partial F_2}{\partial \vec{q_1}} + \frac{\vec{p_2}}{m}\frac{\partial F_2}{\partial \vec{q_2}} - \left(\frac{\partial \vec{\phi}_{12}}{\partial \vec{q_1}} + \frac{\partial \vec{\phi}_1^{ext}}{\partial \vec{q_1}}\right)\frac{\partial F_2}{\partial \vec{p_1}} - \left(\frac{\partial \vec{\phi}_{21}}{\partial \vec{q_2}} + \frac{\partial \vec{\phi}_2^{ext}}{\partial \vec{q_2}}\right)\frac{\partial F_2}{\partial \vec{p_2}} \\ = (N-2)\int \left(\frac{\partial \phi_{13}}{\partial \vec{q_1}}\frac{\partial F_3}{\partial \vec{p_1}} + \frac{\partial \phi_{23}}{\partial \vec{q_2}}\frac{\partial F_3}{\partial \vec{p_2}}\right) d\vec{q_3} d\vec{p_3}.\end{aligned} \tag{2.13}$$

Our next objective is to remove the dependence of F_1 on F_2.

To close equation (2.12), we conceive of a gas with certain properties, sometimes called a Boltzmann gas. A Boltzmann gas is characterized by the following conditions:

1. Only binary collisions between particles are considered.
2. Collisions between particles are localized.
3. The inter-particle potential ϕ_{ij} is short-range.

Given the above conditions, the following limits, called the Boltzmann Gas Limit, are applied:

$$\begin{gathered} N \to \infty \\ m \to 0 \\ b \to 0 \\ Nb^2 = \text{constant} \\ Nm = \text{constant}, \end{gathered} \tag{2.14}$$

where b characterizes the interaction distance between particles. The physical interpretation of the above conditions is the following: the number of particles N in the system is very large and is taken to approach infinity. The masses of the particles are sufficiently small and approach zero such that $Nm =$ constant. The volume of the action sphere of a particle, Nb^3, is sufficiently small that b approaches zero in such a way that $Nb^2 =$ constant and Nb^3 approaches zero, and thus inter-particle forces are neglected. Note that the mean free path is proportional to $1/Nb^2$ so in this limit the mean free path is finite and, in this sense, collisions play a role in the gas dynamics. However,

the limits of a Boltzmann gas describe a perfect gas in the thermodynamic sense, and in a perfect gas the inter-particle forces are neglected because the space occupied by the particles is taken to be vanishingly small.

Following the method of Grad [29] and applying the Boltzmann Gas Limit, we treat binary collisions considering only the pre-collisional states and post-collisional states of particles. We additionally move from considering generalized momentums $\vec{p}_i$ to generalized velocities $\vec{v}_i = \vec{p}_i/m$ and assume particle motions to be in a state of *molecular chaos*. These assumptions allow equation (2.12) to be recast as a closed equation for F_1. Writing now F_1 as f_1 and $\vec{q}_1$ as $\vec{x}_1$, we have

$$\frac{\partial f_1}{\partial t} + \vec{v}_1 \cdot \frac{\partial f_1}{\partial \vec{x}_1} + \frac{1}{m}\frac{\partial \phi_1^{ext}}{\partial \vec{x}_1} \cdot \frac{\partial f_1}{\partial \vec{v}_1} = \left(\frac{\partial f_1}{\partial t}\right)_{coll}, \tag{2.15}$$

where $(\partial f_1/\partial t)_{coll}$ is the collision integral, which represents the contribution of binary collisions to the time-rate of change of f_1. Equation (2.15) is the Boltzmann equation, first derived by Ludwig Boltzmann in 1872, and describes the statistical behavior of a Boltzmann gas. Considering elastic collisions of particles of type 1 with particles of type 2, the collision integral can be written as

$$\left(\frac{\partial f_1}{\partial t}\right)_2 = \int\int\int |\vec{v}_1 - \vec{v}_2|\sigma(\vec{v}_1, \vec{v}_2; \vec{v}_1{}', \vec{v}_2{}')\,(f_1' f_2' - f_1 f_2)\, d^3\vec{v}_2 d^3\vec{v}_1{}' d^3\vec{v}_2{}', \tag{2.16}$$

where $|\vec{v}_1 - \vec{v}_2|$ is the magnitude of the velocity of particle species 1 relative to the velocity of particle species 2, $\sigma(\vec{v}_1, \vec{v}_2; \vec{v}_1{}', \vec{v}_2{}')$ is the collision cross-section as a function of the pre-collision velocities and the post-collision velocities which are denoted by primes, f_2 is the distribution for particle species 2, and the primed and un-primed f refers to the pre-collision and post-collision distribution for a particle species, respectively.

2.1.3 Macroscopic Plasma Properties

Several macroscopic or volume-averaged properties can be calculated by taking moments of the distribution f, where for now we have dropped the subscript on f for simplicity. Taking the

zeroth moment gives the particle number density n,

$$n = \int f d^3\vec{v}. \tag{2.17}$$

Taking the first moment gives the particle flux density $\vec{\Gamma}$,

$$\vec{\Gamma} = \int \vec{v} f d^3\vec{v}. \tag{2.18}$$

The bulk (macroscopic) velocity, $\vec{u}$, can then be calculated from

$$\vec{u} = \frac{\vec{\Gamma}}{n}. \tag{2.19}$$

Taking the second moment gives the total particle energy density ϵ,

$$\epsilon = \frac{1}{2} m \int |\vec{v}|^2 f d^3\vec{v}. \tag{2.20}$$

Assuming an isotropic Maxwellian for three degrees of freedom, the total particle energy density can also be written as

$$\epsilon = \frac{3}{2} n k_B T + \frac{1}{2} n m |\vec{u}|^2. \tag{2.21}$$

Rearranging, the temperature T can then be calculated,

$$T = \frac{2}{3} \frac{\epsilon}{n k_B} - \frac{1}{3} \frac{m|\vec{u}|^2}{k_B}. \tag{2.22}$$

2.1.4 The H-Theorem

Returning to the subscript notation to differentiate particle species, the following functional of f_1 can be introduced,

$$H = \int f_1 \ln f_1 d^3\vec{v}_1. \tag{2.23}$$

Boltzmann's H-theorem states that H can only decrease until the system reaches a state of equilibrium. The time-rate of change of H is

$$\frac{dH}{dt} = \int (1 + \ln f_1) \left(\frac{\partial f_1}{\partial t} \right)_{coll} d^3\vec{v}_1. \tag{2.24}$$

For $(\partial f_1/\partial t)_{coll}$ we can substitute the collision integral from equation (2.16), which can be written as

$$\frac{dH}{dt} = \int\int\int\int (1 + \ln f_1)\, g\sigma \left(f_1' f_2' - f_1 f_2 \right) d^3\vec{v}_1 d^3\vec{v}_2 d^3\vec{v}_1{}' d^3\vec{v}_2{}', \tag{2.25}$$

where we have dropped the parenthesis associated with σ and written $|\vec{v}_1 - \vec{v}_2| = g$. An important property of the collision integral for the elastic binary collisions considered here is that it is symmetric. This allows for the integral to remain the same regardless of whether particle type subscripts 1 and 2 are switched, and also regardless of whether the primed and un-primed values are switched. This property allows equation (2.25) to be rewritten as

$$\frac{dH}{dt} = \frac{1}{4} \int\int\int\int g\sigma \ln \left(\frac{f_1 f_2}{f_1' f_2'} \right) \left(f_1' f_2' - f_1 f_2 \right) d^3\vec{v}_1 d^3\vec{v}_2 d^3\vec{v}_1{}' d^3\vec{v}_2{}'. \tag{2.26}$$

Notice that if $f_1' f_2' - f_1 f_2$ positive, then $\ln\left(f_1 f_2 / f_1' f_2'\right)$ is negative, and if $f_1' f_2' - f_1 f_2$ is negative, then $\ln\left(f_1 f_2 / f_1' f_2'\right)$ is positive. Thus, equation (2.26) can never be positive,

$$\frac{dH}{dt} \leq 0. \tag{2.27}$$

If H can only decrease, then the system must reach equilibrium when H reaches a minimum, or $dH/dt = 0$. This is achieved when

$$f_1 f_2 = f_1' f_2', \tag{2.28}$$

or, taking the natural logarithm of equation (2.28),

$$\ln f_1 + \ln f_2 - \ln f_1' - \ln f_2' = 0. \tag{2.29}$$

Equation (2.29) shows that $\ln f_i$ is summation invariant, which can be written as a linear combination of the summation invariants of f_i, which are the particle number density, momentum, and energy,

$$\ln f_i = a_i + \vec{b}_i \cdot m\vec{v}_i + c_i m|\vec{v}_i|^2, \tag{2.30}$$

where a_i, $\vec{b}_i$, and c_i are constants. Equation (2.30), along with the constraints given by equations (2.17), (2.18), and (2.20), can be used to solve for a_i, $\vec{b}_i$, and c_i. The resulting form for f_i is known as the Maxwell-Boltzmann or Maxwellian distribution,

$$f_M = n\left(\frac{m}{2\pi k_B T}\right)^{3/2} \exp\left(-m\frac{v_x^2 + v_y^2 + v_z^2}{2k_B T}\right), \tag{2.31}$$

which was first formulated by James Maxwell in 1860. We define the thermal velocity as the root-mean-square velocity of the Maxwellian distribution, $v_{th} = \sqrt{df k_B T/m}$, where df here is the number of translational degrees of freedom.

2.1.5 The Vlasov Equation

If we consider the external forces in equation (2.15) to be the Coulomb force, then, for an unmagnetized plasma, the force potential ϕ^{ext} can be written in terms of the electrostatic field $\vec{E}$ (see equation 2.10),

$$\frac{\partial \phi^{ext}}{\partial \vec{x}} = q\vec{E}, \tag{2.32}$$

where q is the electric charge of the particle. Note that ϕ^{ext} is not exactly equivalent to the electrostatic potential ϕ, where $-\partial\phi/\partial\vec{x} = \vec{E}$. The time evolution of a charged particle distribution under the action of electrostatic forces and elastic binary collisions is then given by the form of the Boltzmann equation,

$$\frac{\partial f}{\partial t} + \vec{v} \cdot \frac{\partial f}{\partial \vec{x}} + \frac{q\vec{E}}{m} \cdot \frac{\partial f}{\partial \vec{v}} = \left(\frac{\partial f}{\partial t}\right)_{coll}. \tag{2.33}$$

If the plasma is sufficiently ionized such that the frequency of elastic binary collisions is much less than the characteristic plasma frequency, the right-hand side can be neglected and equation (2.33)

written as

$$\frac{\partial f}{\partial t} + \vec{v} \cdot \frac{\partial f}{\partial \vec{x}} + \frac{q\vec{E}}{m} \cdot \frac{\partial f}{\partial \vec{v}} = 0. \tag{2.34}$$

This is known as the Vlasov equation and is used to describe collisionless plasmas. Though close-range interactions are neglected, the particles are still able to exhibit long-range collective interactions via the Coulomb force, which is accounted for by the electric field $\vec{E}(\vec{x})$. The electric field can be decomposed into an applied field $\vec{E}_{\text{appl}}(\vec{x})$ and a local field $\vec{E}_{\text{local}}(\vec{x})$, so that

$$\vec{E}(\vec{x}) = \vec{E}_{\text{appl}}(\vec{x}) + \vec{E}_{\text{local}}(\vec{x}).$$

The local field results from charge density inhomogeneities in the plasma and can thus be calculated from Gauss's Law,

$$\frac{\partial \vec{E}_{\text{local}}(\vec{x})}{\partial \vec{x}} = \frac{e}{\varepsilon}(n_i - n_e), \tag{2.35}$$

where ε is the electric permittivity tensor. We will always assume a local electric field, so the subscript will be dropped from here onward. For an electrostatic field, we substitute $-\partial\phi/\partial\vec{x} = \vec{E}$ to get Poisson's equation:

$$\nabla^2\phi = -\frac{e}{\varepsilon_0}(n_i - n_e). \tag{2.36}$$

2.1.6 Plasmas as Fluids

Treating a plasma as a continuum is useful for developing predictive computational models of plasma devices due to the efficiency for computation. If the plasma is sufficiently collisional such that relaxation to thermal equilibrium occurs much more quickly than other relevant physical time scales, then the velocity distribution f for each species can be assumed to take the Maxwellian form of f_M in equation (2.31) and the fluid equations for conservation of mass, momentum, and energy can be derived by taking moments of the Boltzmann equation.

The conservation of mass for any species expressed as a continuity equation is

$$\frac{\partial n}{\partial t} + \nabla \cdot (n\vec{u}) = \dot{n}, \tag{2.37}$$

where $\dot{n}$ is the net rate of production of that species through collisions and ∇ is the spatial gradient operator. For example, if the species is an ion, then the right-hand side represents the production of that species of ion through ionization processes. The equation for conservation of momentum in the absence of magnetic fields is

$$mn\left[\frac{\partial \vec{u}}{\partial t} + (\vec{u}\cdot\nabla)\,\vec{u}\right] = qn\vec{E} - \nabla p - mn\nu\vec{u}, \tag{2.38}$$

where p is the pressure, typically calculated using the ideal gas assumption

$$p = nk_B T, \tag{2.39}$$

and $\nu = nv\sigma$ is the collision frequency which is assumed to be constant. The equation for conservation of energy is

$$\frac{\partial \epsilon}{\partial t} + (\vec{v}\cdot\nabla)\,\epsilon = \nabla\cdot(\kappa\nabla T) + \vec{v}\cdot\nabla p + qn\vec{E}\cdot\vec{v} + S, \tag{2.40}$$

where κ is the thermal conductivity tensor and S is a term encompassing the energy gains and losses due to collisions. The equations for total particle energy density and ideal gas, equations (2.21) and (2.39) respectively, can be used to rewrite equation (2.40). After substitution and combining the pressure gradient term with the left-hand side, the energy equation is

$$\frac{\partial}{\partial t}\left(\frac{3}{2}p + \frac{1}{2}m|\vec{u}|^2\right) + (\vec{u}\cdot\nabla)\left(\frac{5}{2}p + \frac{1}{2}m|\vec{u}|^2\right) = \nabla\cdot(\kappa\nabla T) + qn\vec{E}\cdot\vec{u} + S. \tag{2.41}$$

If equation (2.38) is taken to be the electron momentum equation, and if only collisions between electrons and singly-charged ions are considered, the last term in equation (2.38) can be written as $-mn\nu_{ei}\,(\vec{u}_e - \vec{u}_i)$. Physically, because this term arises due to Coulomb collisions, this term is proportional to e^2, the density of electrons n_e and the density of ions $n_i \approx n_e$. This term can thus also be written as $-\eta e^2 n^2\,(\vec{u}_e - \vec{u}_i)$ where η is called the resistivity. Comparing these two forms,

the resistivity can be written as

$$\eta = \nu_{ei}\frac{m}{ne^2}. \tag{2.42}$$

2.2 Plasma Waves

Waves in plasmas are driven by density inhomogeneities and thermal motions of the charged particles. In the absence of close-range collisions, information can be transmitted among particles via the long-range Coulomb force. The two most fundamental plasma frequencies are given by oscillations of the electrons and ions. These frequencies can easily be derived from applying a perturbation theory to the ion and electron momentum equations coupled with Poisson's equation.

Electrons displaced from a uniform, stationary background of ions will feel a restoring force towards nearby opposite charges. The electrons will overshoot and again feel a force drawing them back towards the ions. If thermal motions are neglected, the frequency of this oscillatory motion of the electrons is called the electron plasma frequency,

$$\omega_{pe} = \sqrt{\frac{ne^2}{\varepsilon_0 m_e}}, \tag{2.43}$$

where ε_0 is the permittivity of free space. Including thermal motions, this oscillatory information will be transmitted to neighboring layers of the plasma, and the oscillatory motion becomes a proper wave motion, called electron plasma waves or Langmuir waves. The frequency of electron plasma waves includes a correction to the electron plasma frequency that accounts for the thermal motions,

$$\omega^2 = \omega_{pe}^2 + \frac{3}{2}k^2 v_{th,e}^2.$$

This is the dispersion relation for electron plasma waves, which gives the frequency ω as a function of wavenumber k. Irving Langmuir was among the first to study electron plasma waves in the 1920s.

For electron plasma waves, the ions are assumed uniform and stationary because the ions have much larger inertia than the electrons, and time scales of electron motion are two to three orders

of magnitude faster than ion time scales, depending on the ion mass. However, analogous to how sound waves are transmitted in a gas through particle collisions, ions can transmit information about their motion to neighboring ions through the Coulomb force at the ion plasma frequency,

$$\omega_{pi} = \sqrt{\frac{ne^2}{\varepsilon_0 m_i}}. \tag{2.44}$$

We can use kinetic theory to more generally investigate waves in warm, unmagnetized, collisionless plasmas [30] by considering the Vlasov equation for the electron distribution function f_e with the local electric field given by substituting $-\partial\phi/\partial\vec{x} = \vec{E}$ into Poisson's equation,

$$\frac{\partial f_e}{\partial t} + \vec{v} \cdot \frac{\partial f_e}{\partial \vec{x}} + \frac{q\vec{E}}{m_e} \cdot \frac{\partial f_e}{\partial \vec{v}} = 0, \tag{2.45}$$

$$\frac{\partial \vec{E}}{\partial \vec{x}} = \frac{e}{\varepsilon_0} \left(n_i - \int f_e d^3\vec{v} \right), \tag{2.46}$$

where $n_e = \int f_e d^3\vec{v}$ is the electron number density, and $\vec{E}$ is the local electric field. If we assume that the wave amplitudes are small then we can linearize equations (2.45) and (2.46) by applying a perturbation theory. We split the electron distribution function and electric field into an equilibrium and a perturbed part,

$$f_e(\vec{x}, \vec{v}, t) = f_{e,0}(\vec{v}) + f_{e,1}(\vec{x}, \vec{v}, t), \tag{2.47}$$

$$\vec{E} = \vec{E}_0 + \vec{E}_1, \tag{2.48}$$

where the subscript 0 refers to equilibrium and 1 refers to the perturbation, not to be confused with the subscript representing particles of type 1 in section 2.1.2. The equilibrium electric field is assumed zero due to quasineutrality and the perturbed electric field is a result of local deviations from quasineutrality. The linearized forms of equations (2.45) and (2.46) are

$$\frac{\partial f_{e,1}}{\partial t} + \vec{v} \cdot \frac{\partial f_{e,1}}{\partial \vec{x}} + \frac{q\vec{E_1}}{m_e} \cdot \frac{\partial f_{e,0}}{\partial \vec{v}} = 0, \tag{2.49}$$

$$\frac{\partial \vec{E}_1}{\partial \vec{x}} = -\frac{e}{\varepsilon_0}\int f_{e,1} d^3\vec{v}. \tag{2.50}$$

We now assume that the waves have the form

$$\vec{A} = \vec{A}_0 e^{i(\vec{k}\cdot\vec{x}-\omega t)},$$

where $\vec{A}_0$ is the wave amplitude, $\vec{k}$ is the wave number, and ω is the frequency. The gradient and time derivative of $\vec{A}$ is then $ik\vec{A}$ and $-i\omega\vec{A}$, respectively. Equations (2.49) and (2.50) can then be rewritten as

$$-(\omega - \vec{k}\cdot\vec{v})f_{e,1} + \frac{e\phi_1}{m_e}\vec{k}\cdot\frac{\partial f_{e,0}}{\partial \vec{v}} = 0, \tag{2.51}$$

$$-k^2\phi_1 = \frac{e}{\varepsilon_0}\int f_{e,1} d^3\vec{v}, \tag{2.52}$$

where instead of writing $\vec{E}_1$ we have substituted $\vec{E}_1 = -i\vec{k}\phi_1$. Solving equation (2.52) for ϕ_1 and substituting into equation (2.51) we can write a dispersion relation for electrostatic plasma waves,

$$1 + \frac{e^2}{\varepsilon_0 m_e k^2}\int \frac{\vec{k}\cdot\partial f_{e,0}/\partial\vec{v}}{\omega - \vec{k}\cdot\vec{v}} d^3\vec{v} = 0. \tag{2.53}$$

An obvious problem with this relation is the singularity at $\omega = \vec{k}\cdot\vec{v}$. Lev Landau showed that this can be resolved by treating equation (2.49) as an initial value problem, where the wave is instead assumed to vary sinusoidally in space as

$$\vec{A} = \vec{A}_0 e^{i\vec{k}\cdot\vec{x}},$$

and the time evolution of $f_{e,1}$ is calculated at later times starting from a value specified at $t = 0$. Additionally, we define the velocity parallel to $\vec{k}$ as $v = \vec{v}\cdot\vec{k}/k$, define integrals of $f_{e,0}(\vec{v})$ and $f_{e,1}(\vec{v},t)$ over the velocities perpendicular to $\vec{k}$ as $F_{e,0}(v)$ and $F_{e,1}(v,t)$, respectively, and define

$\vec{E}_1 = E_1\vec{k}/k$. Equations (2.49) and (2.50) can then alternatively be written as

$$\frac{\partial F_{e,1}}{\partial t} + ikuF_{e,1} - \frac{eE_1}{m_e}\frac{\partial F_{e,0}}{\partial v} = 0, \tag{2.54}$$

$$ikE_1 = -\frac{e}{\varepsilon_0}\int F_{e,1}(v)dv. \tag{2.55}$$

We then perform a Laplace transformation of $F_{e,1}$ with respect to t, defined as

$$\bar{F}_{e,1}(v,p) = \int_0^\infty F_{e,1}(v,t)e^{-pt}dt.$$

Equations (2.54) and (2.55) can then be written as

$$p\bar{F}_{e,1} - F_{e,1}(v,t=0) + ikv_e\bar{F}_{e,1} - \frac{e\bar{E}_1}{m_e}\frac{\partial F_{e,0}}{\partial v} = 0, \tag{2.56}$$

$$ik\bar{E}_1 = -\frac{e}{\varepsilon_0}\int \bar{F}_1(v)dv, \tag{2.57}$$

where we have used $\partial F_{e,1}/\partial t = p\bar{F}_{e,1} - F_{e,1}(v,t=0)$. Equations (2.56) and (2.57) can be combined to give

$$ik\bar{E}_1 = -\frac{e}{\varepsilon_0}\int\left[\frac{e\bar{E}_1}{m_e}\frac{\partial F_{e,0}/\partial v}{p+ikv} + \frac{F_{e,1}(v,t=0)}{p+ikv}\right]dv.$$

Solving for $\bar{E}_1$,

$$\bar{E}_1 = -\frac{e}{ik\varepsilon_0\varepsilon(k,p)}\int\frac{F_{e,0}(v,t=0)}{p+ikv}dv,$$

where

$$\varepsilon(k,p) = 1 + \frac{e^2}{\varepsilon_0 m_e k}\int\frac{\partial F_{e,0}/\partial v}{ip-kv}dv. \tag{2.58}$$

$\varepsilon(k,p)$ is the plasma dielectric function, and is well defined because p possesses a positive real part. The roots of the plasma dielectric function give the dispersion relation for electrostatic plasma waves. Landau showed that for $p = -i\omega$, the integral in equation (2.58) can be handled effectively

by careful treatment of the poles during the contour integration in the complex plane.

2.3 Current-Carrying Instability

Current-driven instabilities, i.e., streaming instabilities, take various forms depending on the operating conditions of the plasma [17]. In general, such instabilities are driven by a relative drift between electrons and ions $|u_e - u_i|$ and generate plasma waves that result in an energy exchange between thermal, kinetic, and wave energies.

We can generalize equation (2.58) to account for ion motion by including the Vlasov equation for the ion distribution function f_i in the derivation, giving

$$\varepsilon(k,\omega) = 1 + \frac{e^2}{\varepsilon_0 m_e k}\int \frac{\partial F_{e,0}/\partial v_e}{\omega - k v_e} dv_e + \frac{e^2}{\varepsilon_0 m_i k}\int \frac{\partial F_{i,0}/\partial v_i}{\omega - k v_i} dv_i. \tag{2.59}$$

If we assume the unperturbed electron distribution function to be a shifted-Maxwellian with bulk velocity u_e and ion distribution function to be Maxwellian with bulk velocity $u_i = 0$,

$$F_{e,0} = n\left(\frac{m_e}{2\pi k_B T_e}\right)^{1/2} \exp\left(-m_e \frac{(v_e - u_e)^2}{2k_B T_e}\right), \tag{2.60}$$

$$F_{i,0} = n\left(\frac{m_i}{2\pi k_B T_i}\right)^{1/2} \exp\left(-m_i \frac{v_i^2}{2k_B T_i}\right), \tag{2.61}$$

then the dispersion relation can be written in terms of the plasma dispersion function $Z(\zeta)$,

$$2(k\lambda_D)^2 = Z'(\zeta_e) + Z'(\zeta_i), \tag{2.62}$$

where $\zeta_e = (\omega/k - u_e)/\sqrt{2}v_{th,e}$ and $\zeta_i = \omega/k\sqrt{2}v_{th,i}$, and we have defined the electron and ion thermal velocities to be $v_{th,e} = \sqrt{k_B T_e/m_e}$ and $v_{th,i} = \sqrt{k_B T_i/m_i}$, respectively. We are interested in the asymptotic behaviors of this dispersion relation in various limits that may correspond to the linear growth and nonlinear saturation conditions of the ion acoustic instability.

We can use the assumptions $|\zeta_e| \ll 1$ and $|\zeta_i| \gg 1$ to simplify the plasma dispersion function [31]. Using $\omega_r/k \approx c_s$, the ion condition, $\zeta_i = \sqrt{T_e/2T_i} > 1$, is generally satisfied when

$T_e \gg T_i$. On the other hand, the electron condition can be written as $0 < u_e \ll \sqrt{2}v_{th,e} + c_s$.

If the electron drift is absent, $u_e = 0$, the linear dispersion relation can be written as,

$$1 + \frac{1}{(k\lambda_D)^2} - \frac{\omega_{pi}^2}{\omega^2} = 0, \tag{2.63}$$

where $\lambda_D = \sqrt{\epsilon_0 k_B T_e / e^2 n_e}$ is the Debye length. The solution of this dispersion relation results in $\omega_r^2 \approx k^2 c_s^2$ in the limit of $k\lambda_D \ll 1$ (large wavelength modes). Thus, there is no growth rate but the phase velocity based on the real frequency has two solutions as,

$$\frac{\omega_r}{k} \approx \pm c_s, \tag{2.64}$$

which indicates that the ion acoustic waves propagate isotropically in both directions, i.e., *forward* and *backward*-propagating waves.

If we allow for an electron drift $u_e \neq 0$ we are lead to a linear dispersion relation [15, 30] that results in

$$\frac{\omega_r}{k} \approx +c_s, \tag{2.65}$$

and

$$\frac{\gamma_L}{\omega_r} \approx \sqrt{\frac{\pi}{8}} \left[M - \sqrt{\frac{m_e}{m_i}} - \left(\frac{T_e}{T_i} \right)^{3/2} \exp\left(-\frac{T_e}{2T_i} \right) \right], \tag{2.66}$$

where ω_r is the real part of the frequency, $M = u_e / v_{th,e}$ is the electron Mach number, and $c_s = \sqrt{k_B T_e / m_i}$ is the ion acoustic speed. For the range of M values of interest, e.g., $M \gtrapprox 1$, the electron-to-ion mass ratio can be neglected. Since the phase velocity only has a positive root, the waves propagate only in the *forward* direction, i.e., the same direction as the electron drift. This growth rate is valid only when $\gamma_L / |\omega_r| \ll 1$ [30]. The minimum threshold of M for the current-driven instability to grow ($\gamma_L > 0$) can be calculated from equation (2.66) as,

$$M > M_{\min} = \left(\frac{T_e}{T_i} \right)^{3/2} \exp\left(-\frac{T_e}{2T_i} \right). \tag{2.67}$$

Using equation (2.67), the linear growth rate in equation (2.66) is valid only when $M_{\min} < M \ll \sqrt{2}$ (because $c_s \ll v_{th,e}$ for realistic mass ratio) and $T_e/T_i \gg 1$.

The Buneman instability [32, 33] occurs in the limit of a large electron Mach number, $u_e \gg v_{th,e}$. The ion temperature must be much lower than the electron temperature otherwise significant ion Landau damping will occur. Thus, relative to the electron drift, the particle VDFs approach delta functions. The linear dispersion relation of the Buneman instability is given by

$$1 = \frac{\omega_{pe}^2}{(\omega - ku_e)^2} - \frac{\omega_{pi}^2}{\omega^2}, \tag{2.68}$$

with real frequency

$$\frac{\omega_r}{k} \approx \frac{u_e}{2}\left(\frac{m_e}{2m_i}\right)^{1/3}. \tag{2.69}$$

The linear growth rate is largest at the resonance condition, $ku_e \approx \omega_{pe}$,

$$\frac{\gamma_L}{\omega_{pe}} \approx \frac{\sqrt{3}}{2}\left(\frac{m_e}{2m_i}\right)^{1/3}\left[1 - \frac{1}{2}\left(\frac{m_e}{2m_i}\right)^{1/3}\right]. \tag{2.70}$$

It should be noted that the limit for the Buneman instability, $M_0 \gg 1$, is not explicitly investigated in our simulations, which have maximum $M_0 = 2.5$. Rather, our simulations focus on the transition region from the linear instability $M_0 \leq 1.2$ to the large M_0 that approaches Buneman behavior of rapid growth and plasma heating.

Buneman describes an anomalous resistivity resulting from the field-free ($E_0 = 0$ and $B_0 = 0$) electron-ion two-stream instability, where the electron current supplies the energy to amplify small density perturbations into growing plasma waves. During the growth of a current-driven instability, the relative drift velocity between electrons and ions decreases, while electrostatic potential energy and thermal energy of the electrons and ions increase. After a few plasma periods ω_{pe}^{-1} the field fluctuations have grown large enough that major nonlinear effects become important: (i) anomalous resistivity, (ii) anomalous ion and electron heating, (iii) frequency and growth rate modulation, (iv) mode coupling, and (v) ion and electron trapping. Harmonics of the fundamental mode grow

rapidly, which steepen the potential profile and facilitate the trapping of particles that otherwise would not be achievable at the corresponding potential amplitudes and significantly modifies the particle distributions.

Growth of the instability ceases when the energy input to the wave growth from the relative drift velocity between electrons and ions is balanced by the energy loss by turbulent heating of the plasma. The turbulent heating of the plasma implies that the "cold plasma" approximation of Buneman eventually breaks down. Under certain conditions, the Buneman instability can relax into the ion acoustic instability as the plasma is turbulently heated. Electrons are the first to respond to the instability due to their low inertia so that electron trapping results in a departure from the initial linear growth, indicated by a flattening of the electron distribution around the phase velocities of the ion acoustic waves. A nonlinear dispersion relation is derived by Bartlett [34] adding the nonlinear effects of mode coupling to the quasilinear theory and successfully predicts this effect. However this nonlinear dispersion relation fails to predict the nonlinear saturation. Ishihara and Hirose [35] expand from Bartlett's method to derive an improved nonlinear dispersion relation that is able to successfully predict the field energy at which nonlinear saturation occurs and describes the evolution of the instability before and after electron trapping. While electrons play a vital role in the nonlinear saturation of the instability, it is the ion dynamics that dominate the final saturation and evolution of the instability after nonlinear saturation [36]. Ions resonant with the ion acoustic waves are accelerated to high velocities relative to the bulk ions, resulting in the growth of non-Maxwellian tails on the ion VDF that fluid theory fails to describe. Chapman et al. [37] discuss the decay of ion acoustic waves into solitons and daughter ion acoustic waves via a process called two-ion decay (TID), which may be important in the long-time evolution of the nonlinear saturation.

Quasilinear theory assumes that the mean value of the distribution function, $\langle f \rangle$, varies slowly compared to the growth rate,

$$\frac{1}{\langle f \rangle} \frac{\partial \langle f \rangle}{\partial t} \ll \gamma_L. \tag{2.71}$$

This is valid when the linear growth rate, γ_L, is sufficiently larger than the bounce frequency, $\nu_{B,s} = k\sqrt{e\phi_0/m_s}$, where ϕ_0 is the potential amplitude and m_s is the mass of the species ($s =$

i, e) [38, 39]. The nonlinear saturation process begins when the amplitude of the plasma waves reaches a point where $\nu_{B,s} \gtrapprox \gamma_L$, so that particle trapping dominates the dynamics. The spread in velocity space is often modeled as a diffusive process [40],

$$\frac{\partial f_i}{\partial t} + v\frac{\partial f_i}{\partial v} = \frac{\partial}{\partial v}\left[D_{QL}\frac{\partial f_i}{\partial v}\right], \tag{2.72}$$

where under the quasilinear assumption, the diffusion coefficient D_{QL} is time independent. When the amplitude of the plasma waves become large enough to significantly distort the ion VDFs during the growth process, the condition (2.71) is violated. The changing ion VDF during the growth process will result in a change in the ion Landau damping, which feeds back into the change of the ion VDF. The result is that the quasilinear diffusion operator is time dependent, which affects the long-time evolution of the instability [41].

For a hollow cathode, there is the question of whether the electron drift is able to exceed the threshold velocity for the Buneman instability before the deceleration of the electrons due to turbulent heating at the low M_0 threshold occurs. For an applied electric field, the threshold electric field for the Buneman instability to occur can be written as as [42],

$$E_B = \frac{2m_e c_s \omega_{pe}}{e}.$$

Electrons will accelerate to their thermal velocity during a time

$$t_B \sim \frac{E_B}{2E\omega_{pi}}.$$

The reason the electron acceleration is related to the ion plasma frequency is because the growth rate of the instability depends on the ion dynamics. The time required for an instability to develop is

$$t_{IN} = \sqrt{\frac{m_e c_s}{2\gamma_s e E}},$$

where E is the applied electric field and γ_s is the contribution of the electron drift energy to the

growth rate of the instability. If $t_{IN} > t_B$, the low M_0 instability will not have time to develop, and the electrons will be able to accelerate to $v_{th,e}$. On the other hand, the Buneman instability will occur if

$$\frac{e}{m_e} t_{IN} E \gg v_{th,e}.$$

Quasilinear theory describes quantitatively the emergence of ion acoustic turbulence (IAT) from the current-driven instability at low M_0. However, a consistent theory describing the relaxation of the Buneman instability to IAT requires the dynamics of ion heating, and has yet to be successfully developed [42].

3. 1D VLASOV-POISSON SIMULATION

The simulation codes are set as a representation of the low plasma density region in a hollow cathode plume a few millimeters downstream of the cathode keeper plate where recent growth models have shown maximum anomalous resistivity [13, 27], and where it is postulated that the high-energy ions linked to cathode erosion are generated.

The Vlasov equation for one spatial dimension and one velocity dimension (1D1V) is solved for the electrons and ions, respectively,

$$\frac{\partial f_e}{\partial t} + v_e \frac{\partial f_e}{\partial x} - \frac{eE(x)}{m_e}\frac{\partial f_e}{\partial v_e} = 0, \tag{3.1}$$

and

$$\frac{\partial f_i}{\partial t} + v_i \frac{\partial f_i}{\partial x} + \frac{eE(x)}{m_i}\frac{\partial f_i}{\partial v_i} = 0. \tag{3.2}$$

A description of the solver can also be found for previous studies such as Ref. [24]. Electrons are initialized as a shifted Maxwellian distribution with a range of initial bulk velocities $u_{e,0}$,

$$f_{e,0} = n_{e,0}\sqrt{\frac{1}{2\pi v_{th,e}}}\exp\left[-\frac{(v_e - u_{e,0})^2}{2v_{th,e}}\right], \tag{3.3}$$

where $n_{e,0}$ is the initial electron number density, the electron thermal velocity is defined as $v_{th,e} = \sqrt{eT_{e,0}/m_e}$ with initial electron temperature $T_{e,0} = 2$ eV. The ions are initialized as a stationary Maxwellian distribution

$$f_{i,0} = n_{i,0}\sqrt{\frac{1}{2\pi v_{th,i}}}\exp\left[-\frac{v_i^2}{2v_{th,i}}\right], \tag{3.4}$$

where $n_{i,0}$ is the initial ion number density, the ion thermal velocity is defined as $v_{th,i} = \sqrt{eT_{i,0}/m_i}$ with initial ion temperature $T_{i,0} = 0.2$ eV, thus for the initial condition $T_{e,0}/T_{i,0} = 10$.

The electric field is found as $E(x) = -\partial\phi/\partial x$. Using a Fast Fourier Transform with a tridiagonal matrix solver algorithm with periodic boundary conditions, the 1D Poisson's equation is

solved to calculate the potential,

$$\frac{\partial^2 \phi}{\partial x^2} = -\frac{e}{\varepsilon_0}(n_i - n_e). \tag{3.5}$$

The electron and ion number densities are calculated by taking the zeroth moment of the 1D VDF of each species,

$$n_e = \int f_e(v_e) dv_e, \tag{3.6}$$

and

$$n_i = \int f_i(v_i) dv_i. \tag{3.7}$$

The initial condition is that of a quasineutral plasma, $n_{e,0} = n_{i,0} = n_0$. To facilitate initiation of the instability, a seed perturbation is added for the initial ion number density profile,

$$n_{i,0}(x) = n_0(1 + \mathrm{RNG} \times 10^{-12}), \tag{3.8}$$

where RNG is a random number generator for a number between 0 and 1, up to 6 significant figures.

This system is solved in a discretized phase space, illustrated in Figure 3.1, using a finite volume method with Monotonic Upwind Scheme for Conservation Laws (MUSCL) framework with Aurora-Roe limiter [24]. The numerical flux is 2nd order accurate and the stencil depends on the sign of the velocity. For the left face of cell [i], if the velocity is positive the stencil utilizes cells [i-1], [i], and [i+1], and if the velocity is negative it uses [i], [i+1], and [i+2]. For the right face of cell [i], if the velocity is positive the stencil utilizes cells [i-2], [i-1], and [i], and if the velocity is negative it uses [i-1], [i], and [i+1].

Two physical domain lengths are considered that allow the excitation of multiple wave modes: the first being $L_1 = 130\lambda_D$, which is the case for the majority of the simulation results, and the second being $L_2 = 260\lambda_D$, to consider the effects of the domain size on the wave dynamics. The number of spatial cells is 1,024 for L_1 and 2,048 for L_2 to keep the cell size constant. There are 2,400 velocity bins for electrons and 1,800 velocity bins for the ions, and the velocity space is taken

as $v/v_{th,e} \in [-8, 8]$ and $v/v_{th,i} \in [-36, 36]$ for electrons and ions, respectively. Strang's time-splitting scheme is used to split the time iteration for the electrons and ions due to the difference between time scales of their motion [43]. The time step for the ion motion is $\Delta t = 10$ ps, the electron timestep is $\Delta t_e = \Delta t/120$, and the maximum run time is 5 μs to ensure the solution at nonlinear saturation reaches a steady state in the average.

Most hollow cathode experiments and numerical simulations in which anomalous transport and erosion are studied utilize xenon (mass of 131 amu) as the propellant species. With computation time considered, especially in a DK simulation, the primary ion species for this study was chosen to be singly-charged Argon (mass of 40 amu). Singly-charged xenon ions were also used in additional cases for $M_0 = 1.5$, 2.0, and 2.5 in order to study the dependence of instability growth and saturation on ion mass.

The current I is held at a constant 30 A so that the initial bulk velocity $u_{e,0}$ can be modified by

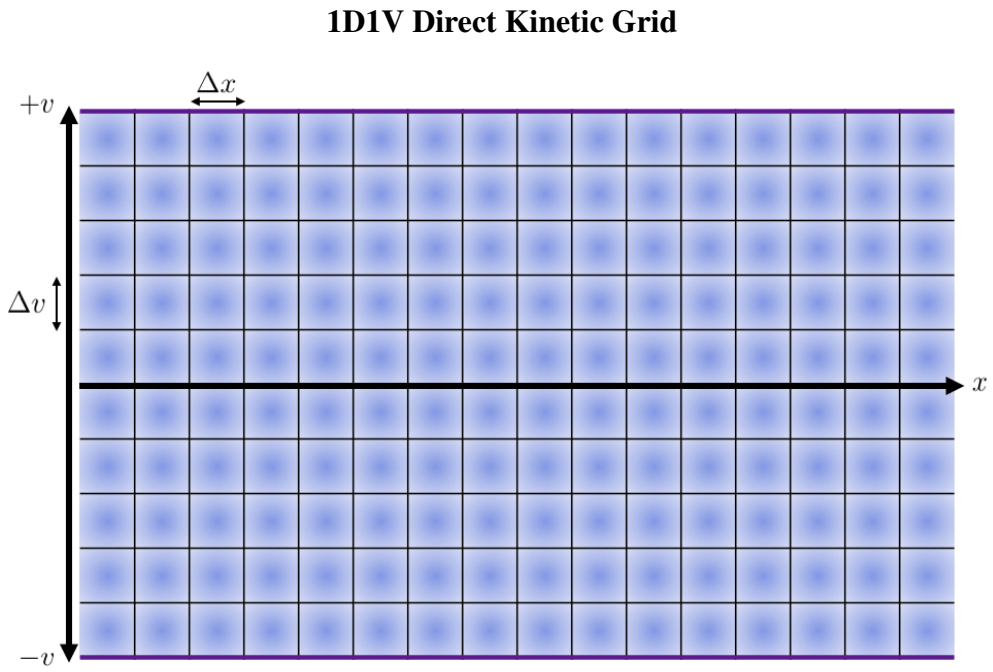

Figure 3.1: Illustration of the phase space grid used for the 1D1V Vlasov-Poisson solver.

changing the initial plasma density n_0. Thus, the initial electron bulk velocity is determined as,

$$u_{e,0} = \frac{I}{en_0\pi R^2}, \tag{3.9}$$

where $R = 3$ mm is the bulk plasma radius assuming minimal expansion from the cathode orifice. This allows for simulations to be initialized with different initial electron Mach numbers, $M_0 = u_{e,0}/v_{th,e0}$. The initial electron Mach number is chosen to vary from 0.5 to 2.5. The lower limit of 0.5 is chosen to show the linear regime and the upper limit of 2.5 is chosen as an arbitrary cutoff for studying the nonlinear regime.

The code utilizes Message-Passing Interface (MPI) for parallelization. Figure 3.2 shows speedup vs number of processors for various grid sizes. The speedup is calculated as

$$\text{Speedup} = \frac{\text{W}_{\text{serial}}}{\text{W(S)}}, \tag{3.10}$$

where S is the number of processors. The base grid size is that used for these simulations; 1,024 spatial cells, 1,800 ion velocity bins, and 2,400 electron velocity bins. The coarse grid consists of half the number of spatial cells and velocity bins as the base grid, and the fine grid consists of twice the number of spatial cells and velocity bins as the base grid. The speedup for the coarse grid followed a linear profile up to approximately 25-36 processors. The base and fine grids followed a linear profile up to approximately 64-81 processors. The reason the speedup for the base grid appears to be super-linear is probably due to cache limitations for the serial run and run with four processors. The base grid was chosen with 64 processors for moderate run time while maintaining the highest resource efficiency, and a single simulation runs for 2-3 days with 64 processors on the Ada cluster at the High Performance Research Computing facility in Texas A&M University. Matlab was used for all of the post-processing analysis and generation of the figures in the results section.

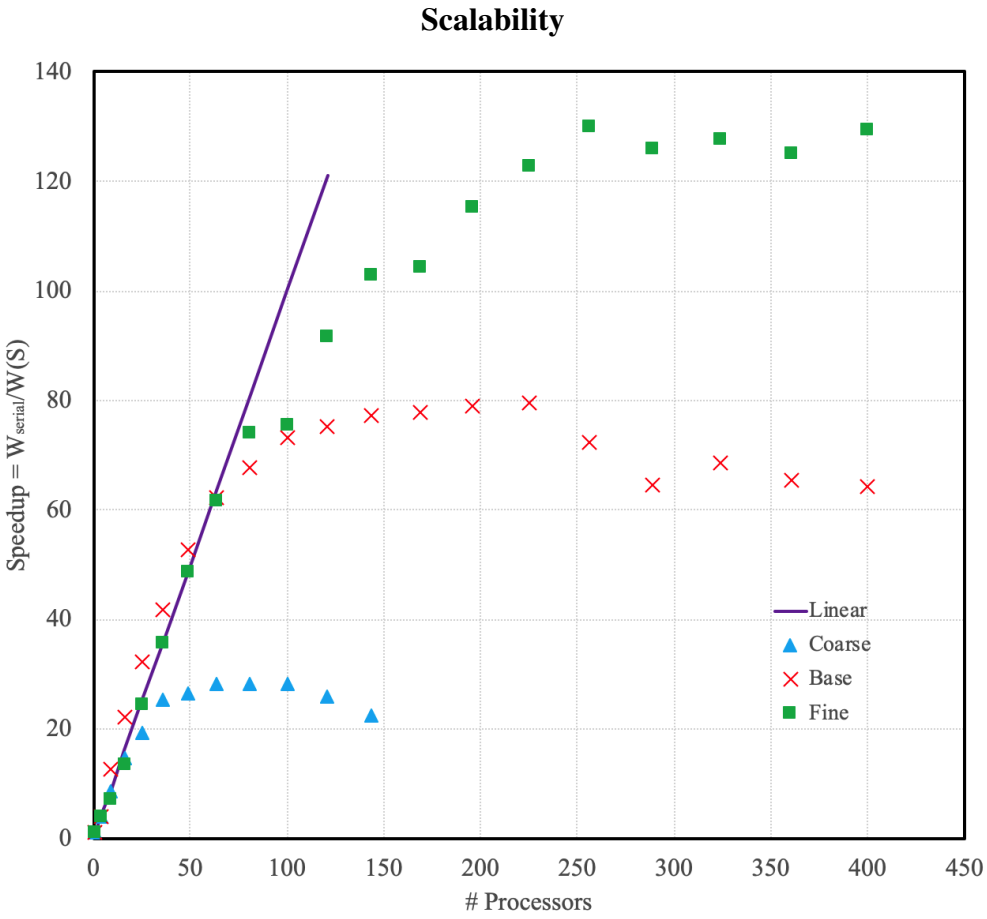

Figure 3.2: Speedup versus number of processors for Coarse (512 spatial cells, 900 ion velocity bins, and 1,200 electron velocity bins), Base (1,024 spatial cells, 1,800 ion velocity bins, and 2,400 electron velocity bins), and Fine (2,048 spatial cells, 3,600 ion velocity bins, and 4,800 electron velocity bins) grid resolutions.

4.1 Linear Growth and Nonlinear Saturation

Figure 4.1 shows the wave number spectrum of the potential profile during the linear growth phase for $0.5 \leq M_0 \leq 2.5$, calculated from a discrete Fast Fourier Transform of the spatial potential profile. The y-axis is scaled to allow better differentiation between the different M_0 cases, and is not meant to indicate a particular potential amplitude, although generally the larger the M_0 the greater the potential amplitude. One can see two trends in the wave number spectrum during linear growth as M_0 increases. First, the wavenmumber spectrum is more broad for $0.5 \leq M_0 \leq$

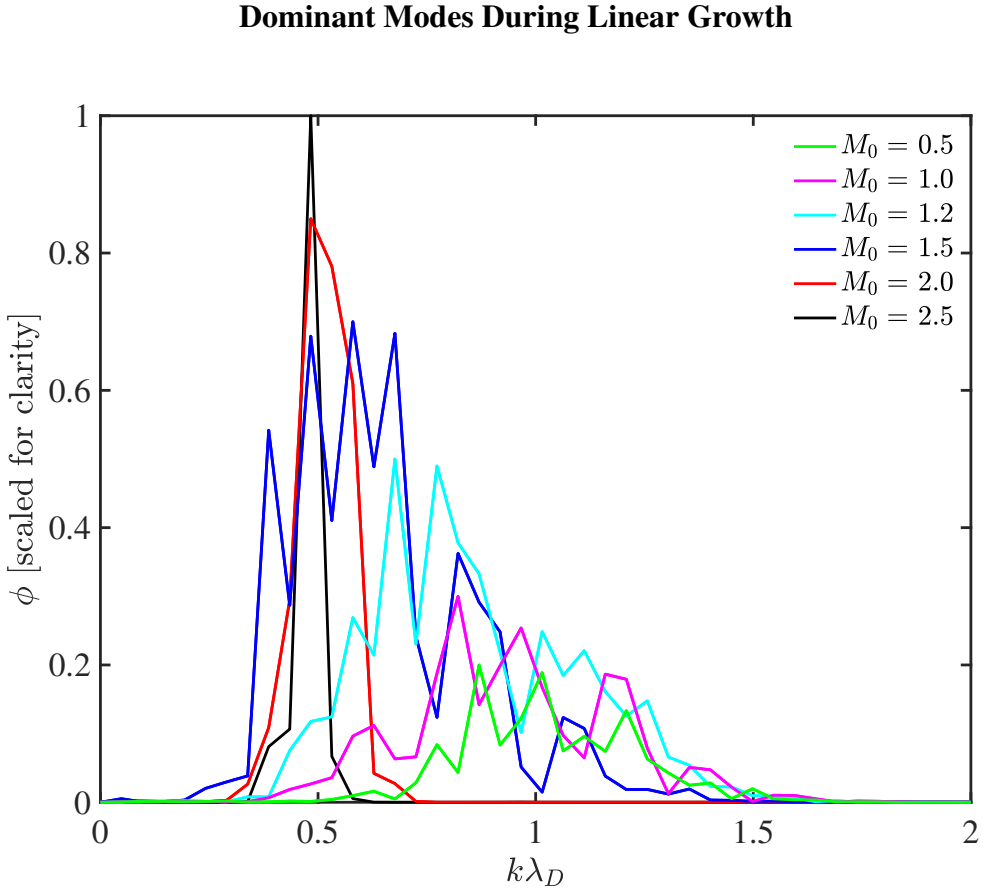

Figure 4.1: Dominant modes of the potential during the linear growth phase for $0.5 \leq M_0 \leq 2.5$. The potential is scaled for clarity and does not reflect relative normalized amplitudes.

1.2. At $M_0 = 1.5$, the spectrum is transitioning to be more confined around lower wave numbers. For $M_0 = 2.0$ and 2.5, the wave number spectrum is shown to approach a single mode. This agrees with the behavior predicted by Stringer for a mass ratio of $m_i/m_e = 1836$ [15]. Second, as M_0 increases the most dominant mode is shown to be decreasing in wave number, with the dominant mode for $M_0 = 0.5$ shown to be $k\lambda_D \approx 0.8 - 1.0$ and the most dominant mode for $M_0 = 2.5$ shown to be $k\lambda_D \approx 0.5$.

Linear Growth and Nonlinear Saturation of Electrostatic Potential Energy (reprinted from Ref. [44] with permission)

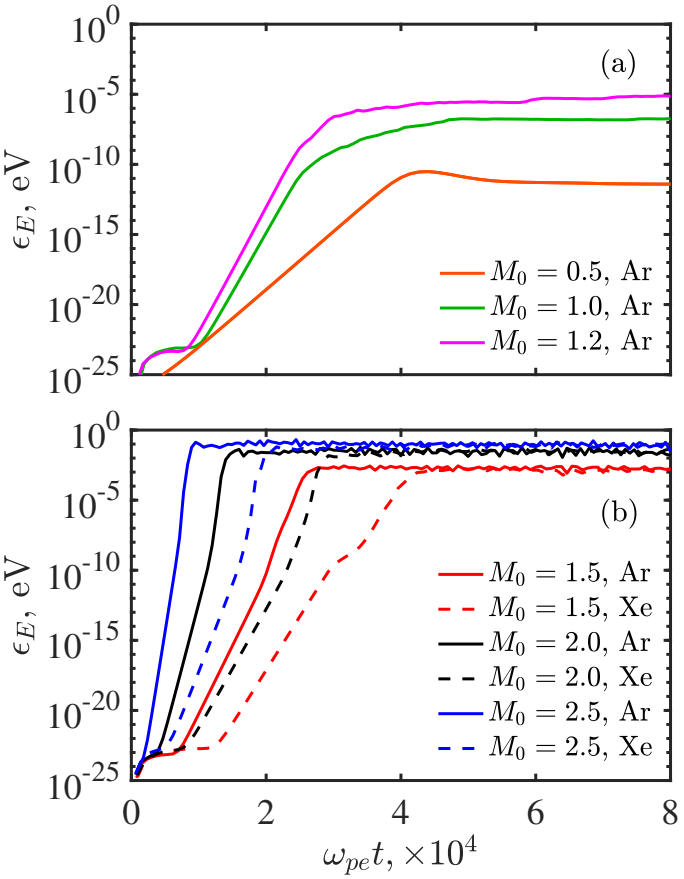

Figure 4.2: Electrostatic potential energy as a function of initial electron Mach number and ion mass, (a) quasilinear regime for argon, and (b) nonlinear regime for argon and xenon. Note that the plasma densities are different for each M_0 since equation (3.9) is used, while $T_{e,0} = 2$ eV, for the numerical simulations. Reproduced from page 4 of Ref. [44]. First published May 21, 2019.

The normalized electrostatic potential energy density in eV is calculated as

$$\epsilon_E = \frac{1}{en_0 L} \int \frac{1}{2} \varepsilon_0 |E|^2 dx. \tag{4.1}$$

Figure 4.2 shows the time evolution of the electrostatic potential energy density through the linear growth and nonlinear saturation phases for $0.5 \leq M_0 \leq 2.5$ for argon and xenon ions. The growth rate from the simulation results can be calculated by taking the slope as

$$\gamma = \frac{\ln\left[\epsilon_E(t_2)\right] - \ln\left[\epsilon_E(t_1)\right]}{t_2 - t_1}. \tag{4.2}$$

A comparison of the growth rates calculated from the linear theory using equation (2.66) and from the simulation using equation (4.2) are shown in Table 4.1. During the linear growth phase, the growth rate increases as M_0 increases, and is on the same order as value predicted from linear theory, with good agreement for $M_0 = 0.5$. For $M_0 = 0.5$, the simulation gives $\gamma/\omega_r = 0.16$ while equation (2.66) gives $\gamma_L/\omega_r = 0.18$. Even at low M_0, $\zeta_i = \mathcal{O}(1)$ and $\zeta_e = \mathcal{O}(10^{-1} - 1)$ under the parameters assumed in these simulations, while in the linear theory it is assumed that $\zeta_i \gg 1$

Growth Rate Comparison

M_0	Eq. (2.66)	Eq. (4.2)
Argon (40 amu)		
0.5	0.18	0.16
1.0	0.49	0.24
1.2	0.62	0.28
1.5	0.81	0.41
2.0	1.12	1.11
2.5	1.43	2.08
Xenon (131 amu)		
1.5	0.81	0.66
2.0	1.12	1.04
2.5	1.43	2.00

Table 4.1: Comparison of the growth rates calculated from the linear theory using equation 2.66 and from the simulation using equation 4.2.

Time Evolution of the Longest Wavelength Modes

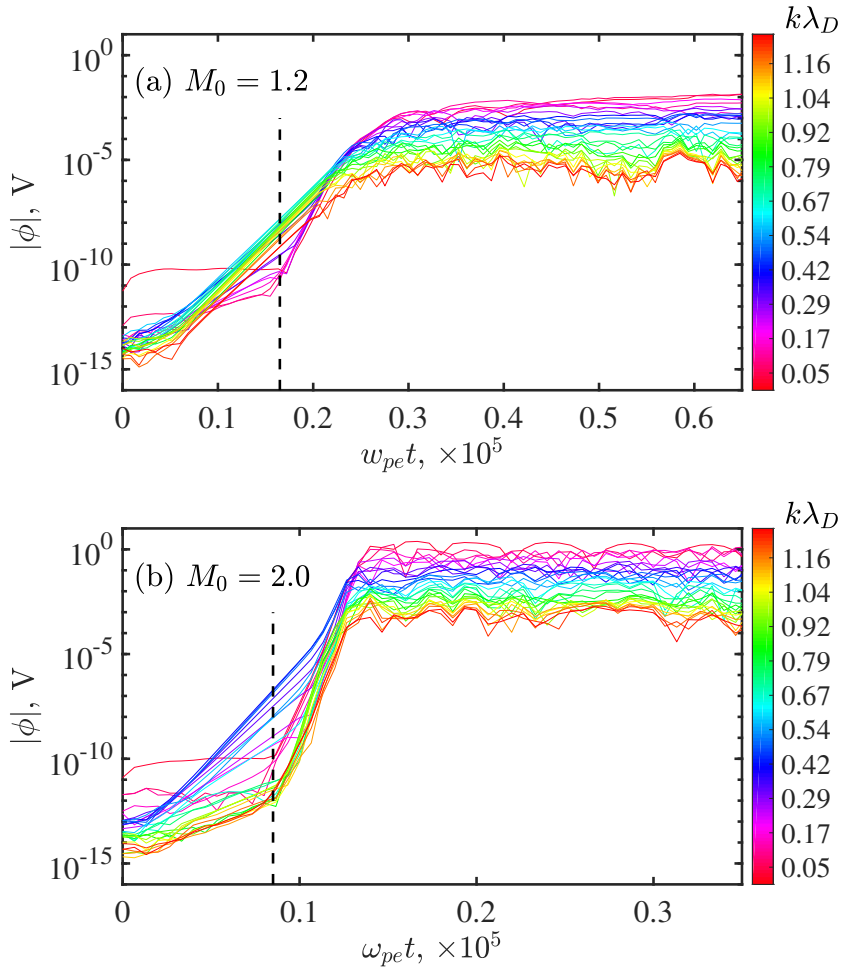

Figure 4.3: Growth of the thirty longest-wavelength modes in the wave number spectrum for (a) $M_0 = 1.2$ and (b) $M_0 = 2.0$. Note the change in scale for $\omega_{pe}t$ between the two cases. Black dotted line indicates transition where the modes that dominate nonlinear saturation begin their most rapid growth.

and $\zeta_e \ll 1$. Equation (2.66) seems to over predict the growth rate for $1.0 \leq M_0 \leq 2.0$, and for $M_0 > 2.0$ the growth rate from the simulation begins to show larger values. These discrepancies are expected because nonlinear effects become more significant as M_0 increases when $\gamma \ll \omega_r$ is no longer satisfied. For the low M_0 cases there is a transition phase between the linear growth and saturation phases because the potential amplitude is small, so the characteristic time for ion trapping is large. The increase in the saturated wave energy with M_0 is nonlinear, with the saturated

wave energy being 5 orders of magnitude larger for $M_0 \geq 2$ than for $M_0 = 1$. Additionally, one can see that increasing the ion mass delays the saturation due to the increase in the bounce period, while the final saturation energy is relatively independent of the ion species. The final saturation energy was shown by Ishihara et al. [35] to scale very weakly with the ion mass, $\approx 0.1W_0$ and $0.16W_0$ for hydrogen and xenon, respectively, where W_0 is the initial electron drift energy.

Figure 4.3 shows the growth of the thirty longest-wavelength modes for $M_0 = 1.2$ and 2.5. The growth profile agrees very well qualitatively with the results of driven waves undergoing two-ion decay (TID) in [37]. TID was discussed as a mechanism for the generation of subharmonic ion acoustic waves from parent ion acoustic waves, and Ref. [37] shows the formation of ion solitary waves as a result of this process. It can be seen that the the k modes that end up dominant during nonlinear saturation have the largest growth rates during the linear growth phase, and that this growth doesn't occur for the most dominant k modes until all around the same time indicated by the vertical dashed black lines. This shows clearly that the energy in the k mode that is dominant during the linear growth and predicted by the linear theory relaxes into longer wavelength modes during nonlinear saturation.

4.1.1 Quasilinear regime

Figure 4.4 shows the VDFs of electrons and ions for $M_0 = 1.2$ at 3 μs ($\omega_{pe}t = 5.3 \times 10^5$) in the nonlinear saturation phase. One can see there is very little electron and ion trapping around the phase velocity, $v_\phi = \omega_r/k \approx 5v_{th,i} \approx +1.5c_s$, and the VDFs remain essentially Maxwellian with a small perturbation component. This agrees with the current-driven instability theory as shown in Equation (2.66), which predicts that the trapping occurs only in the same direction as the electron drift. The amplitude of the plasma wave is not large enough to perturb the electrons and ions to initiate an ion acoustic wave in both directions. Nonlinear effects here are sufficiently weak that the overall dynamics can be described using the linear theory. It can be seen from Figure 4.4(b) that high energy ions up to 20 eV ($v \approx 10v_{th,i}$) are generated at the nonlinear saturation stage. A possible acceleration mechanism for these ions beyond the phase velocity is related to changes in the ion sound speed due to ion heating and nonlinear effects. It was shown in Ref. [38] that

Electron and Ion VDFs in the Quasilinear Regime (reprinted from Ref. [44] with permission)

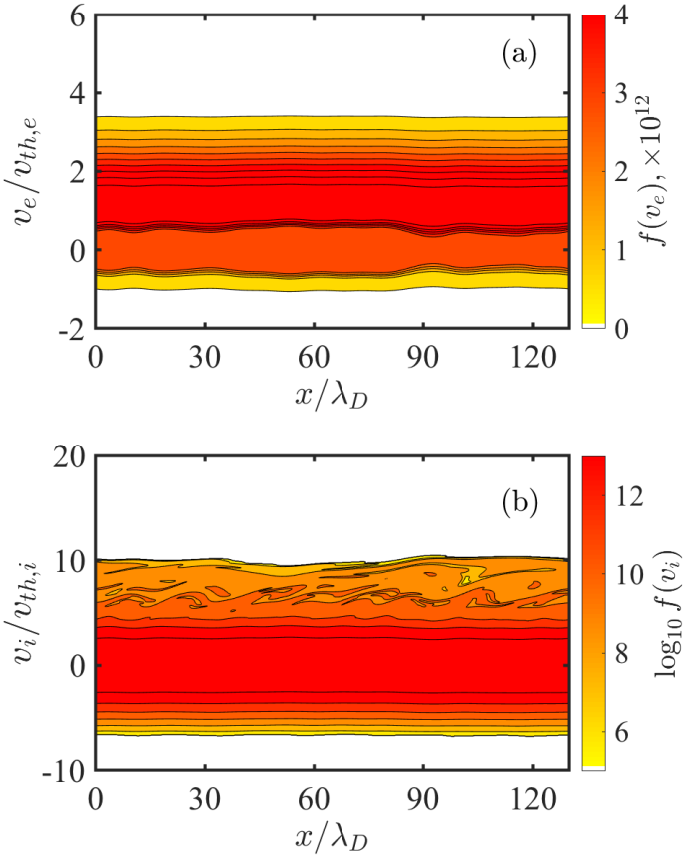

Figure 4.4: Velocity distributions for $M_0 = 1.2$ (quasilinear regime) at 3 μs ($\omega_{pe}t = 5.3 \times 10^5$): (a) electrons and (b) ions. Note that ion VDF is shown in logarithmic scale. Reproduced from page 5 of Ref. [44]. First published May 21, 2019.

nonlinear plasma frequency shift can occur due to trapping of ions and electrons, which increases the phase velocity of ion acoustic waves for $T_e/T_i \gg 1$.

4.1.2 Nonlinear regime

Figure 4.5 shows the spatially averaged electron and ion VDFs for $M_0 = 2$ at (a) 100 ns $\leq t \leq$ 300 ns for the electrons and (c) 110 ns $\leq t \leq$ 500 ns for the ions, as well as the instantaneous VDFs of electrons and ions for $M_0 = 2$ at $t = 150$ ns ($\omega_{pe}t = 2\times10^4$) in (b) and (d). A quasi-steady state is reached by the ions some time between 300-500 ns. At $t = 100$ ns, the electrons are being

Electron and Ion VDFs in the Nonlinear Regime (reprinted from Ref. [44] with permission)

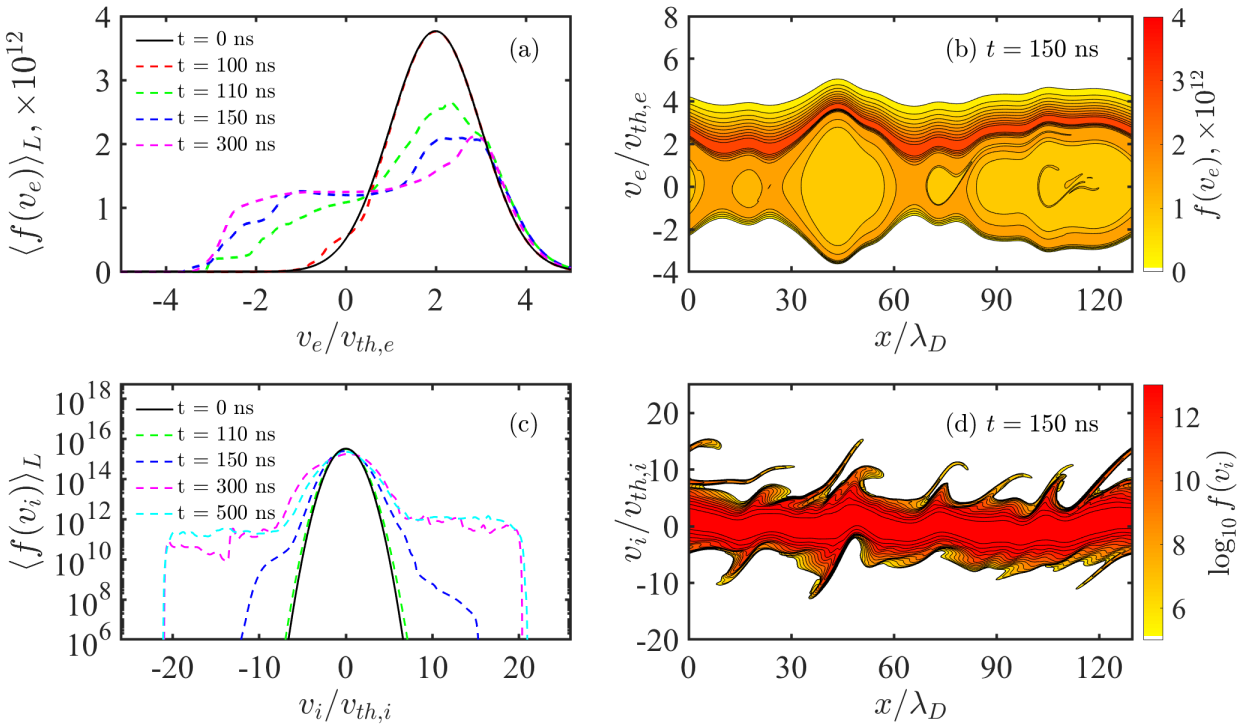

Figure 4.5: Velocity distributions for $M_0 = 2.0$ during the final stage of linear growth and the beginning of nonlinear saturation (see Fig. 4.2): (a) spatially-averaged electron VDFs for 0 ns, 100 ns, 110 ns, 150 ns, and 300 ns, (b) instantaneous electron VDF at 150 ns, (c) spatially-averaged ion VDFs (in logarithmic scale) for 0 ns, 100 ns, 110 ns, 150 ns, 300 ns, and 500 ns, and (d) instantaneous ion VDF (in logarithmic scale) at 150 ns. Reproduced from page 6 of Ref. [44]. First published May 21, 2019.

trapped with relatively large potential amplitude, while it takes time for the trapping to occur based on the bounce frequency, as can be seen from Figure 4.2. The trapped electrons, shown in Figures 4.5(a) and 4.5(b), significantly reduces the bulk velocity of electrons since $u_e(t) = \int v\hat{f}_e(v)dv$, where $\hat{f}_e(v) = f_e(v)/n_e$ is the normalized VDF. This is the *collisionless* scattering that results in anomalous resistivity of the electron current.

Some fraction of the electron population from the bulk VDF moves in the negative velocity due to trapping in the forward-propagating ion acoustic waves. The velocity of such backstreaming electrons which originate from the bulk of the electron VDF can be given by $u_{e,\mathrm{neg}} = -\sqrt{e\phi_0/m_e}$. It was hypothesized in Ref. [44] that the backstreaming electrons may serve as a source of a sec-

ondary current-driven instability in the direction opposite to the primary instability, provided that $M_{e,\text{neg}} = -u_{e,\text{neg}}/v_{th,e} = -\sqrt{\phi_0/T_e}$ must be large enough [15]. It may be this secondary instability that results in plasma waves propagating with negative velocity, and combined with the initial current-driven instability lead to the appearance of forward and backward ion acoustic wave propagation.

4.2 Anomalous Resistivity

Figure 4.6 shows the time evolution of the spatially-averaged (a) electron Mach number M, (b) electron temperature T_e, and (c) ion temperature T_i for $1.0 \leq M_0 \leq 2.5$. One can see that the growth of large amplitude plasma waves significantly reduce the electron bulk velocity and simultaneously increases the electron temperature as shown in Figure 4.6(b), leading to a reduction in the electron Mach number, $M = u_e/v_{th,e}$ as shown in Figure 4.6(a). The time rate change of the bulk velocity, $du_e/dt = -\nu_{\text{eff}} u_e$, is relatively constant for $M_0 \leq 1.2$. However, for $M_0 \geq 1.2$, ν_{eff} varies over time, which can be seen from the drastic change in electron Mach number, $M = u_e/v_{th,e}$, when nonlinear saturation occurs after the linear instability. The electron and ion temperatures are calculated from equation (2.22) applied to one spatial dimension. The electron temperature is shown to increase up to $6T_{e,0} = 12$ eV for $M_0 = 2.5$. Probe measurements from Jorns et al. [23] have shown electron temperatures in the hollow cathode plume on the order of $1 - 3$ eV. Measurements of the electron temperature experiments must be carefully investigated when the electron VDFs are highly non-Maxwellian.

Figure 4.6(c) shows little increase in the ion temperature for $M_0 \leq 1.7$, but beyond $M_0 = 2.0$ the ion heating becomes significant. As will be shown later, this reflects the fact that the bulk of the ion VDF is largely unaffected by the plasma waves until when M_0 approaches 2.0. The growth of tails in the ion VDF indicating the formation of high energy ions will have relatively little effect on the ion temperature calculation, which illustrates the inability of fluid models to accurately capture the effects of high energy ions unless the ion kinetics are properly incorporated into the models. It can also be seen that the ion temperature is slow to increase compared to the electron temperature after the instability has saturated. This is due to the slow inertial response of the heavy ions to the

Time Evolution of Plasma Properties (reprinted from Ref. [44] with permission)

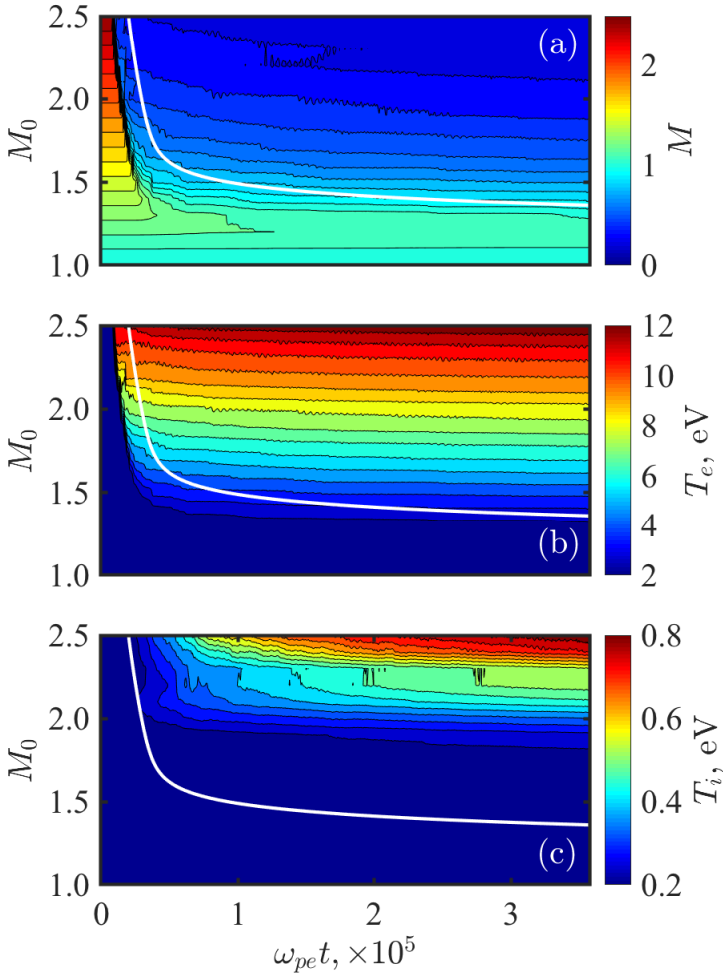

Figure 4.6: Time evolution of (a) electron Mach number M, (b) electron temperature T_e, and (c) ion temperature T_i, over the range $1.0 \leq M_0 \leq 2.5$. Solid white line shows the time at which $f(v_i)$ in the negative tail of the ion VDF is not less than 10^{-6} below the bulk of the ion VDF for the velocities $v_i < -6v_{th,i}$. Reproduced from page 6 of Ref. [44]. First published May 21, 2019.

instability. It should be noted that ion Landau damping does occur as a saturation mechanism, but this is not immediately translated into ion heating.

The solid white lines through Figure 4.6 indicate the time where the population of backstreaming high-energy ions has become significant, which is based on observation, and is defined as the time at which $f(v_i)$ in the negative tail of the ion VDF is not less than 10^{-6} below the bulk of the ion VDF for the velocities $v_i < -6v_{th,i}$.

Jorns et al. calculated the electron Mach number to be $M \approx 0.14$ from experimental measurements of T_e and n_e during steady state operation in a 140 A LaB_6 hollow cathode [5]. However, steady state operation is after the instability has already saturated, and our numerical results show that the electron Mach number during saturation can be significantly different than the initial condition that determines the growth rate of the instability. If the plasma wave is large during the growth of the instability, then quasilinear theory is no longer applicable, and all knowledge of the initial condition that led to the growth of the instability is lost once saturation occurs. Ishihara et al. [35] pointed out that the initial growth happens so rapidly that it is essentially impossible to measure the temporal growth rate from experiments, and that the only identifiable frequency from measurements is a slow oscillation comparable to the ion plasma frequency. This presents a significant problem in using experimental data to model anomalous electron transport due to current-driven instabilities for numerical simulations. One idea is to use the knowledge of M from experiments or in simulations, which corresponds to the saturation regime, to extrapolate back to a likely initial value of M_0, and the true nature of the instability growth can be estimated. For example, based on Figure 4.6, if $M \approx 0.14$ during saturation then the initial condition M_0 may be greater than 2.5, which led to the generation of large-amplitude plasma waves that decreased M to its saturation value. The nonlinearities that lead to these discrepancies in plasma properties during steady state operation will become more important as current requirements of hollow cathodes as electron sources for high-power ion propulsion become increasingly more demanding [23, 44]. This illustrates the importance of incorporating self-consistent models of plasma kinetics in fluid simulations and the necessity of researching and employing methods that may inhibit the growth of the instability in hollow cathodes [45].

It has been of interest to capture the anomalous electron momentum dissipation due to the growth and saturation of the instability on bulk plasma properties in a fluid formulation. An effective momentum transfer frequency based on quasilinear theory was proposed by Sagdeev [46], which is given by

$$\nu_{\text{eff}} = \alpha \omega_{pe} M \sqrt{\frac{T_e}{T_i}}, \tag{4.3}$$

where $\alpha = \mathcal{O}(10^{-2})$. The Sagdeev model assumes a saturated state of IAT and incorporates electron kinetic effects, but assumes that the ion VDF varies slowly with the growth rate. The result is that nonlinear ion dynamics are ignored during the growth of the instability, which leads to a time independent diffusion operator acting on the ion VDF, because broadening of the ion VDF will influence the diffusion operator. The nonlinear ion dynamics therefore result in a time dependent diffusion operator which affects the long-time evolution of the instability. This means that as M_0 increases and the ion dynamics become more nonlinear during the growth of the instability, the nonlinearly saturated state will deviate further from that predicted by quasilinear theory.

In Ref. [13] an effective collision frequency based on the plasma wave energy was derived and is given by

$$\nu_{\text{eff}} = \alpha\omega_{pe}\frac{\epsilon_E}{T_e}. \tag{4.4}$$

Among the assumptions made in the derivation of this model include a small growth rate $\gamma \ll \omega_r \ll \omega_{pi}$ and a linear dispersion relation. We have shown that the first condition does not hold when M_0 is large, and it is M_0 that determines growth and long-time evolution of the instability, not the value of M during nonlinear saturation, which may become smaller as M_0 increases. The model also neglects nonlinear wave dynamics such as wave-wave and wave-particle coupling since the wave amplitudes cannot become very large before saturation occurs with a small growth rate.

We can take Ohm's Law as

$$\frac{du_e}{dt} = \frac{|e|E}{m_e} - u_e\nu_{\text{eff}}. \tag{4.5}$$

We consider the electric field E as the result of the local deviations from quasineutrality such as what is occurring in these kinetic, field-free simulations. We can write E in terms of the electrostatic potential energy from equation (4.1) as $E = \sqrt{2\epsilon_E e n_e/\varepsilon_0}$. Substituting into Ohm's Law and assuming the saturation state where $du_e/dt \approx 0$, we have

$$\nu_{\text{eff}} = \alpha\frac{\omega_{pe}}{M}\sqrt{\frac{2\epsilon_E}{T_e}}, \tag{4.6}$$

which looks similar in form to the wave growth model in equation (4.4) and we have added $\alpha \approx$

0.01 to account for wave energy going into the electron pressure rather than damping the drift (see Future Work in section 5.2).

Figure 4.7 shows the effective collision frequency for $1.0 \leq M_0 \leq 2.5$ for the three cases

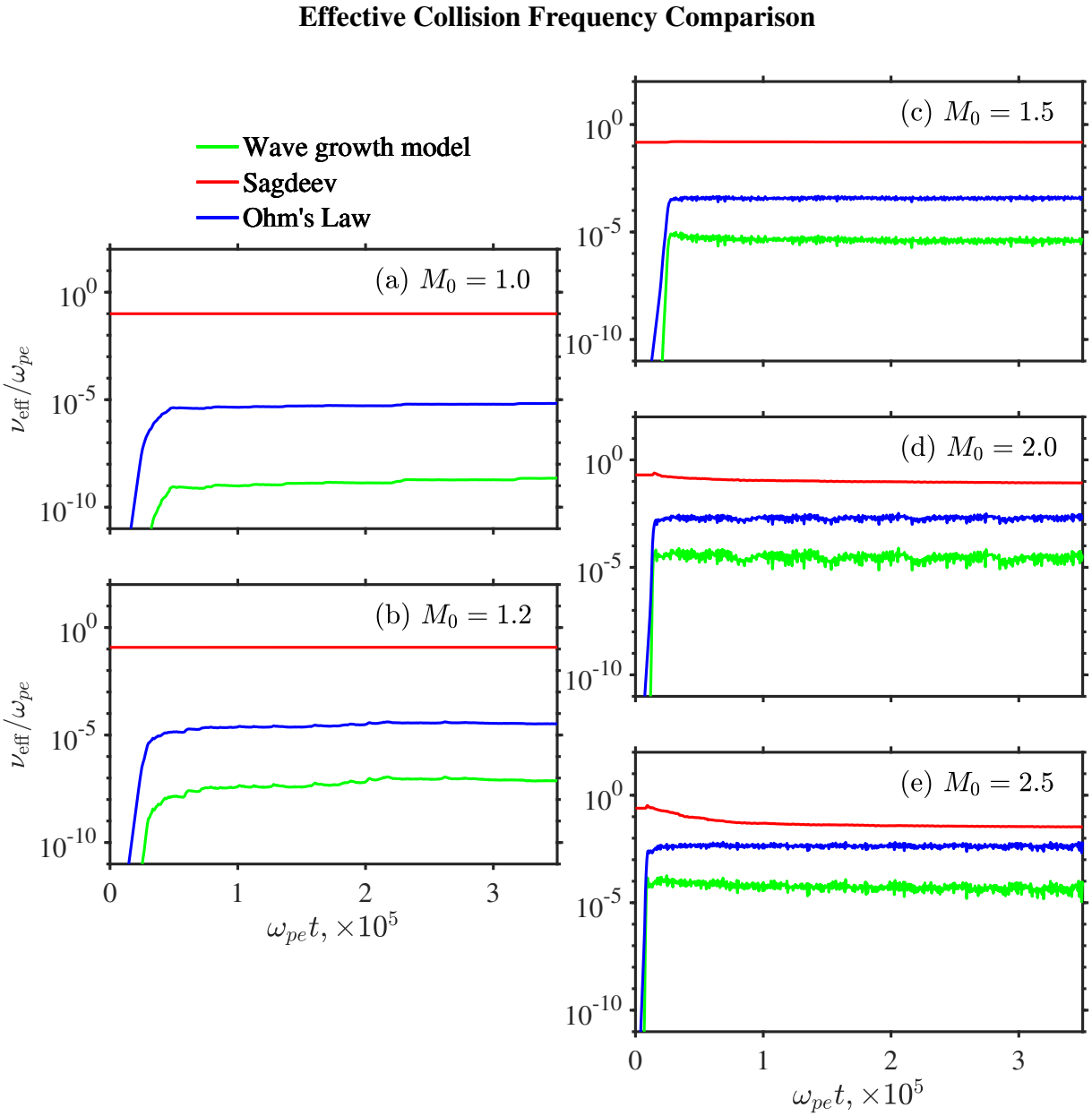

Figure 4.7: Effective collision frequencies resulting from collisionless scattering of electrons, for (a) $M_0 = 1.0$, (b) $M_0 = 1.2$, (c) $M_0 = 1.5$, (d) $M_0 = 2.0$, (e) $M_0 = 2.5$. All are calculated with the same value of $\alpha = 0.01$.

described above: equations (4.4), (4.3), and (4.6). One can see that the value for ν_{eff} calculated with the Sagdeev model doesn't significantly change across different M_0. This is because M and T_e/T_i don't appreciably change between the different cases in terms of order of magnitude. However, the effective collision frequency calculated from the Sagdeev model actually decreases during saturation as M_0 increases, which is not in keeping with the upward scaling with M_0 of the electrostatic fluctuations that cause the collisionless scattering. The electrostatic potential energy ϵ_E changes significantly and nonlinearly as M_0 increases, and this is reflected in the results for the wave growth model and the model from equation (4.6), which are qualitatively very similar.

4.3 Potential Fluctuations and Ion Kinetics

Time averages are taken of the ion VDFs after an approximately steady state has been reached, i.e. for $t \geq 2$ μs. The maximum and root-mean-square (RMS) of the potential profile are shown in Figure 4.8(a1)-(e1) and the spatio-temporally averaged ion VDFs for $M_0 = 1.0, 1.2, 1.5, 2.0,$ and 2.5 are shown in Figure 4.8(a2)-(e2).

As was also shown in Figure 4.5(d), one of the most unique features of a large M_0 case is the generation of high-energy ions with negative velocity as shown in Figures 4.8(c2)-(e2). One can see the formation of bi-directional tails in the ion VDF due to the isotropic ion acoustic waves that develop during saturation as M_0 transitions between $1.3 \geq M_0 \geq 1.5$. For $M_0 = 1.0$ shown in Figure 4.8(a), the amplitude of the plasma waves are small $\phi_0 \approx 0.01 - 0.02$ V, and as a result there is very little ion trapping. The case for $M_0 = 1.2$ shown in Figure 4.8(b) is similar to the case for $M_0 = 1.0$, but the amplitude of the plasma waves are larger by a factor of 10, $\phi_0 \approx 0.1 - 0.2$ V, and a larger population of ions are trapped in the plasma waves $n_{i,tr} \approx 10^{10}$ m^{-3} up to a velocity $10v_{th,i}$. In Figure 4.8(c), for $M_0 = 1.5$ the potential again increases by about a factor of 10 compared to the $M_0 = 1.2$ case, $\phi_0 \approx 1 - 2$ V. For this potential amplitude, one can see ion trapping in backward-propagating ion acoustic waves with a trapping population only slightly smaller than population of ions trapped in the forward-propagating ion acoustic waves $n_{i,tr} \approx 10^{11}$ m^{-3}, up to velocities $17v_{th,i}$ in the forward direction and $-15v_{th,i}$ in the backward direction. One can see that for $M_0 = 2.0$ and 2.5, in Figures 4.8(d) and 4.8(e), the population of trapped ions in both

Potential Fluctuations and Ion Kinetics (reprinted from Ref. [44] with permission)

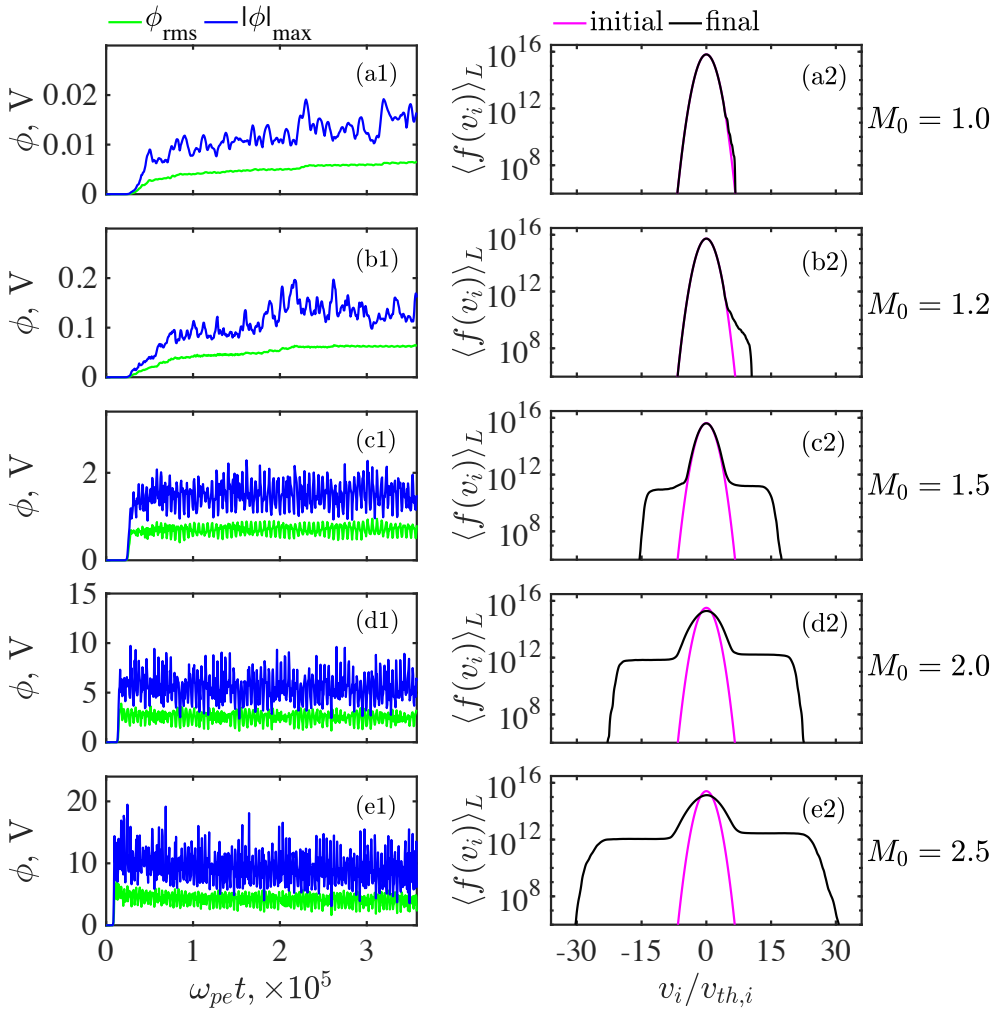

Figure 4.8: Time evolution of maximum and root-mean-square potential (left) and spatiotemporally-averaged ion VDF comparison between initial Maxwellian and nonlinear saturation (right): (a) $M_0 = 1.0$, (b) $M_0 = 1.2$, (c) $M_0 = 1.5$, (d) $M_0 = 2.0$, and (e) $M_0 = 2.5$. Reproduced from page 8 of Ref. [44]. First published May 21, 2019.

the forward- and backward-propagating waves continue to increase $n_{i,tr} \approx 10^{12}$ m^{-3}, extending out to velocities of $22v_{th,i}$ for $M_0 = 2.0$ and $30v_{th,i}$ for $M_0 = 2.5$. Further, it can be seen that the plasma waves now heavily affect the bulk distributions of the ions as the potential amplitudes become comparable to the electron energy, $\frac{1}{2}mu_e^2 + \frac{1}{2}k_B T_{e,0} \approx 3 - 4$ eV, leading to an increase in the ion temperature as shown in Figure 4.6(c). For a sinusoidal potential profile, the ratio of the

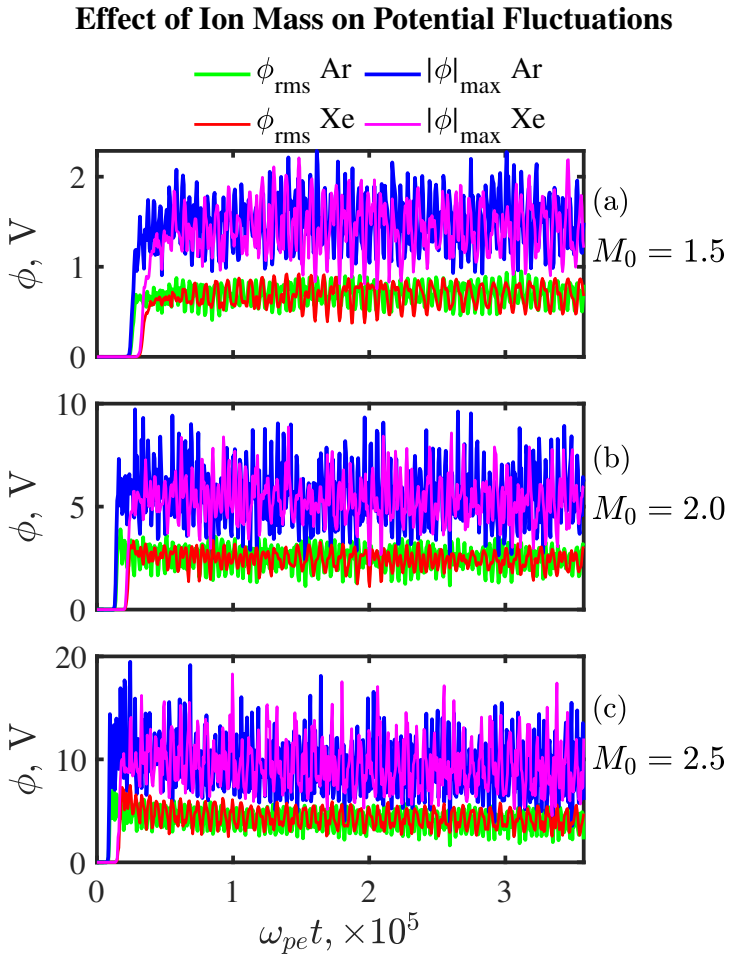

Figure 4.9: Comparison of maximum and root-mean-square potentials for argon (40 amu) and xenon (131 amu) for $M_0 = 1.5$, 2.0, and 2.5.

amplitude to the RMS scales as $\phi_{\max}/\phi_{\rm rms} = \sqrt{2}$. In these results $\phi_{\max}/\phi_{\rm rms} \approx 2-2.5$, suggesting the presence of ion solitary waves with locally high potential amplitudes.

Figure 4.9 shows the effect of ion mass on the maximum and RMS potentials for the cases $M_0 = 1.5$, 2.0, and 2.5 by including simulation results for xenon. While xenon is more than three times heavier than argon, there is little to no difference in the potential fluctuations at large M_0, in agreement with Ref. [35]. Figure 4.10 shows the maximum and RMS of the time average of the spatially-averaged potential for argon as shown in Figure 4.8(a), as a function of the initial electron Mach number, M_0. The larger the maximum potential, the larger the maximum energy the ions

Potential Fluctuation Scaling with Initial Electron Mach Number (reprinted from Ref. [44] with permission)

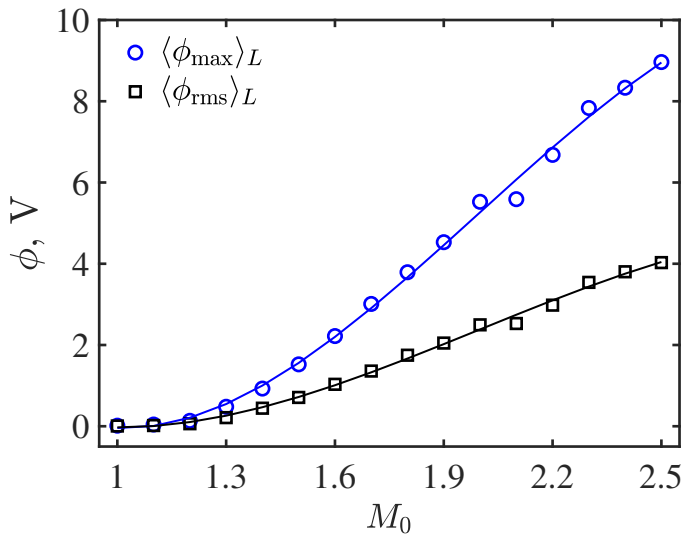

Figure 4.10: Time-averaged maximum and root-mean-square potential as a function of initial electron Mach number, M_0. Symbols are numerical results and lines are cubic fit functions. Reproduced from page 9 of Ref. [44]. First published May 21, 2019. © IOP Publishing. Reproduced with permission. All rights reserved.

can achieve, and the greater the number of ions that are able to be accelerated. The data are fitted to a 3rd-order polynomial in M_0, where the dependence of the maximum and RMS potentials can be approximated as [44]

$$\phi_{\rm max} = 15.59 - 31.18M_0 + 19.97M_0^2 - 3.374M_0^3, \tag{4.7}$$

and

$$\phi_{\rm rms} = 4.886 - 11.02M_0 + 7.331M_0^2 - 1.223M_0^3, \tag{4.8}$$

which are valid for $1.0 < M_0 \leq 2.5$. It has been shown that the potential fluctuations occurring in the cathode plume can couple with the Hall thruster discharge [47, 48], though many fluid and hybrid models of Hall thrusters assume a constant potential profile for the cathode boundary condition [49, 50, 51, 52]. Instead, for a particular set of initial conditions time-varying data can

be input as potential profile boundary conditions during operation for Hall thruster models.

Figure 4.11 shows a closer look at the time evolution of the electrostatic potential energy during nonlinear saturation for $M_0 = 2.0$. In Figure 4.11(a) it is apparent that there is a periodic structure to the time evolution of the electrostatic potential energy with a period of $\omega_{pe}t \approx 6 \times 10^4$. Figure 4.11(b) shows the time evolution of the spatial potential profile. One can clearly see the trajectories of both forward- and backward-running waves, with the phase velocity of a wave given by the magnitude of the slope of the trajectory of that wave. The phase velocity of the plasma waves can be calculated by taking the slope of their trajectory through Figure 4.11(b), with the highest velocity wave giving $v_\phi \approx -8{,}066$ m/s. With the plasma being heated from the instability, we can calculate the warm ion sound speed as

$$c_{s,\mathrm{warm}} = \sqrt{\frac{e}{m_i}\left(\frac{T_e}{1+(k\lambda_D)^2} + 3T_i\right)} \tag{4.9}$$

using the electron and ion temperatures from Figure 4.6. For $T_e \approx 8$ eV and $T_i \approx 0.35$ eV, $c_{s,\mathrm{warm}} \approx 4{,}652$ m/s. This suggests the waves observed in Figure 4.11(a) are ion solitary waves with phase velocity far exceeding the warm ion sound speed, and it is possible that these waves are responsible for extending the high-energy ion tail beyond $c_{s,\mathrm{warm}} + \Delta v_{tr}$ [37]. Figure 4.11(c) shows the time evolution of the electrostatic potential in wave number space, calculated from the the potential in Figure 4.11(b) using a discrete Fast Fourier Transform method. One can see that for a significant portion of the simulation time the majority of the electrostatic potential energy is contained within the mode with wavelength equal to the domain length, $k_{1(1)}\lambda_D = 2\pi/130$ where the subscript (1) refers to the domain size L_1, and from Figure 4.11(a) this energy shows no increase in the average. It can also be observed that the electrostatic potential energy flows throughout higher wave number modes $0.05 \leq k\lambda_D \leq 0.2$. Throughout these periods of energy flow from $k_{1(1)}$ to higher k the electrostatic potential energy is seen to grow steadily as shown in Figure 4.11(a). Following this steady growth the electrostatic potential energy experiences a relatively sharp decrease in energy and the wave number spectrum collapses back down to $k_{1(1)}$

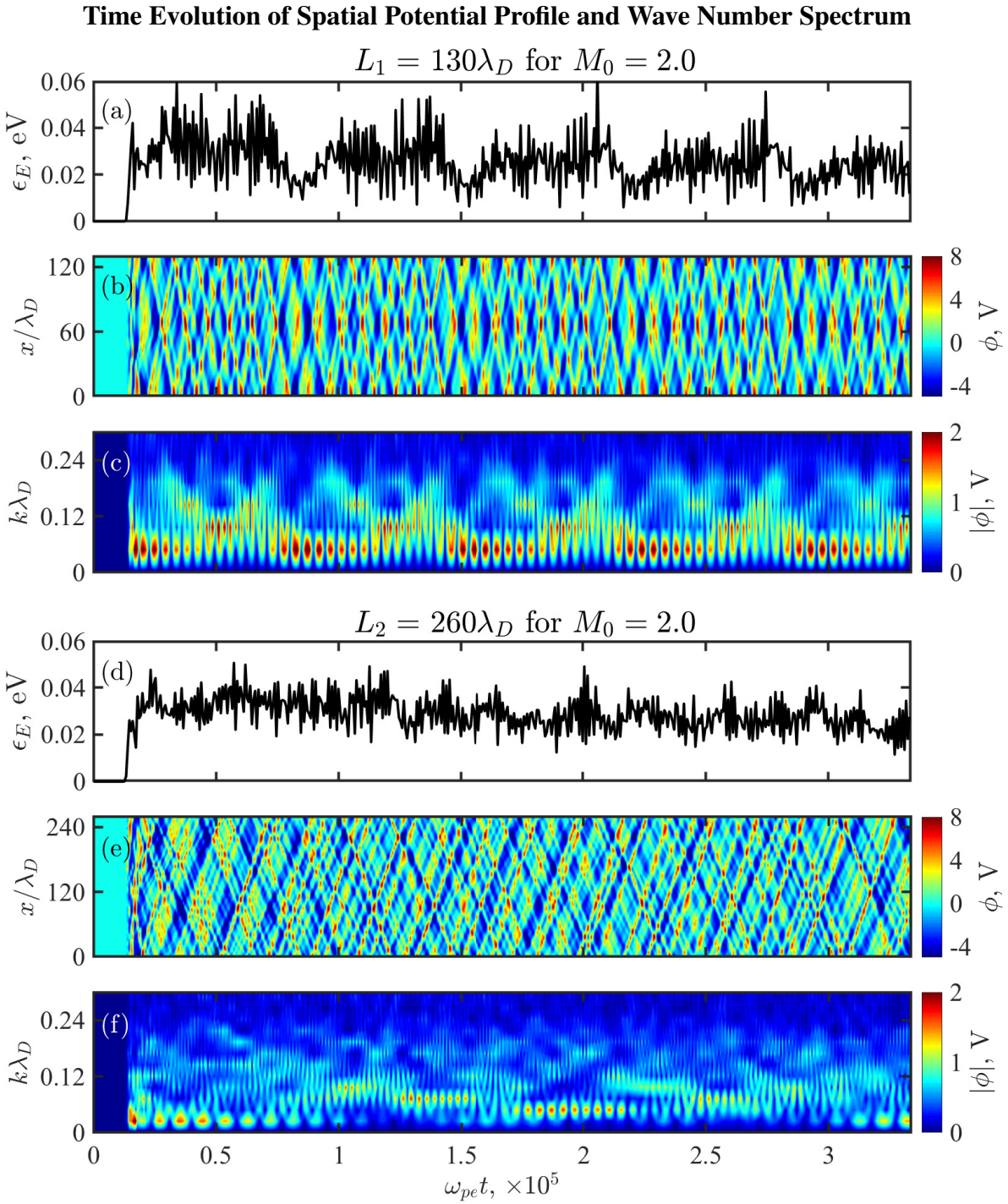

Figure 4.11: Time evolution for $M_0 = 2.0$ of (a) electric field energy, (b) spatial potential profile, and (c) wave number spectrum of the potential for a simulation domain length of $L_1 = 130\lambda_D$, and (d) electric field energy, (e) spatial potential profile, and (f) wave number spectrum of the potential for a simulation domain length of $L_2 = 260\lambda_D$.

and the process starts over. Energy transfer from a fundamental $k_{1(1)}$ to higher k "subharmonic" modes via TID was discussed by Chapman et al. [37] as a mechanism for the generation of IAT and ion solitary waves.

A simulation for $M_0 = 2.0$ with double the domain size was carried out and is shown in Figure 4.11(d)-(f). One can see from Figure 4.11(d) and 4.11(e) that the saturation energy average and phase velocities of the waves are independent of L. Even though the wave energy and phase velocities are the same, Figure 4.11(f) shows a noticeably different time evolution of the wave number profile, though it is expected that the wave number profile should be different for when the simulation domain length is changed. Additionally, the periodic structure to the time evolution of wave energy that was obvious in Figure 4.11(a) is no longer apparent. While the fundamental mode $k_{1(1)}\lambda_D \approx 0.05$ for $L_1 = 130\lambda_D$, the fundamental mode for $L_2 = 260\lambda_D$ is now $k_{1(2)}\lambda_D \approx 0.025$. One can see from Figure 4.11(f) that the electrostatic potential energy is less contained within $k_{1(2)}$ compared to $k_{1(1)}$ in Figure 4.11(c), and also that the energy flow between the different k modes is more complex due to the increased number of available modes in L_2. For both Figures 4.11(c) and 4.11(f), the electrostatic potential energy directly after saturation is mostly contained within $k_{1(1)}$ and $k_{1(2)}$. In Figure 4.11(f), the electrostatic potential energy does not return to $k_{1(2)}$ until around $\omega_{pe}t \approx 3.3 \times 10^5$. It is at this time that the pattern for energy flow between the different wave numbers may start over and a periodic structure in the time evolution of the electrostatic potential energy persists also for $L_2 = 260\lambda_D$, however the simulation run time ended at $\omega_{pe}t \approx 3.3 \times 10^5$ so that cannot be confirmed with these results.

Figure 4.12 shows the wave number spectrum during nonlinear saturation for $M_0 = 1.2$ and $M_0 = 2.0$. It was reported in Ref. [42] that the wave number spectrum in the quasilinear regime scales as $\phi_r \propto k^{-3}\ln[(k\lambda_D)^{-1}]$, which is shown as the red dashed line for $M_0 = 1.2$. Curves are fitted to the wave number spectrum for $M_0 = 2.0$ where $\phi_r \propto \exp(-8k\lambda_D)$ applies for $k\lambda_D < 1.5$ and $\phi_r \propto k^{-4}$ for $1.5 < k\lambda_D < 7$, where ϕ_r and k are the potential amplitude and wave number of the r^{th} mode. Fitted scalings were reported in Ref. [37] of $\phi_r \propto \exp(-3k\lambda_D)$ for $k\lambda_D < 1.5$ and $\phi_r \propto 3k^{-4}$ for $1.5 < k\lambda_D < 7$ for hydrogen ions where the first and second harmonics were

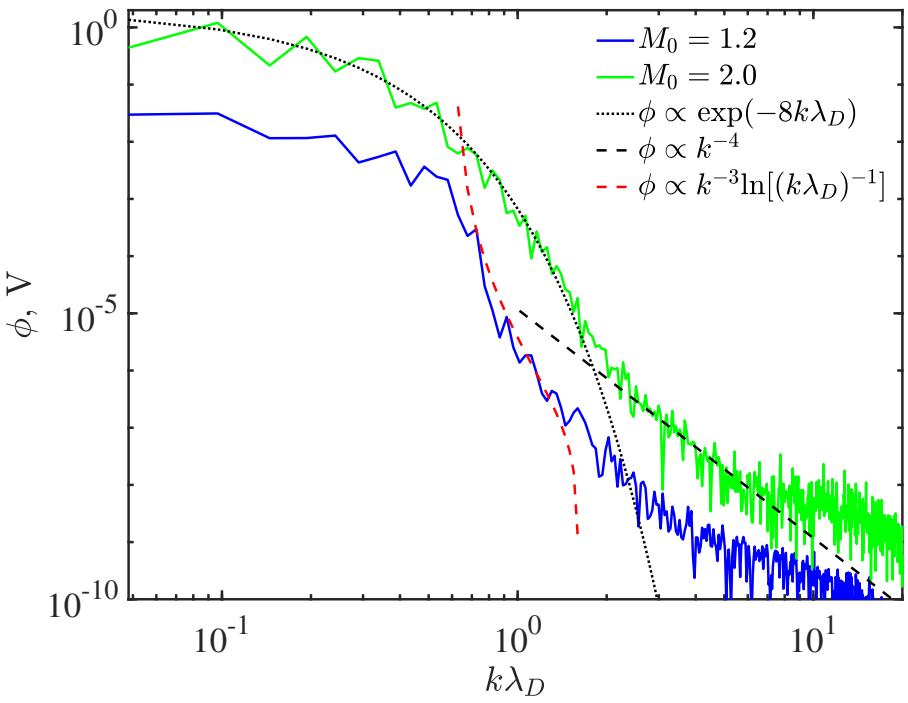

Figure 4.12: Wave number spectrum during nonlinear saturation for (a) $M_0 = 1.2$ and (b) $M_0 = 2.0$. Black dotted and dashed lines are curve fits to the distribution for $M_0 = 2.0$ and the red dashed line is the curve fit for a distribution in the quasilinear regime $M_0 = 1.2$ as reported in [42].

driven by an electric field of $e\lambda_D E_d/T_e = 1 \times 10^{-3}$, while the results presented here are for argon in the field-free case. The scalings are different for longer wavelengths but for lower wavelengths they are the same.

Figure 4.13 shows dispersion diagrams for (a) $M_0 = 1.0$, (b) $M_0 = 1.2$, (c) $M_0 = 1.5$, (d) $M_0 = 2.0$, and (e) $M_0 = 2.5$ for the domain length $L_1 = 130\lambda_D$. For each figure, the horizontal axis is $k\lambda_D$, the vertical axis is ω/ω_{pe}, and the contour color scale is as $\ln|\phi|$. One can see clearly the changing nature of the plasma waves during nonlinear saturation as M_0 is increased, most notable the waves with a negative phase velocity $-\omega/k$ for $M_0 = 1.5$, 2.0, and 2.5. But one can also see that the shape of the dispersion diagram for $M_0 = 1.5$ is more similar to $M_0 = 1.0$ and 1.2, which extend out to higher wave numbers, than to $M_0 = 2.0$ and 2.5, which are more restricted to the lower wave numbers. As M_0 increases, there is less of a wave number dependence on the

Dispersion Diagrams during Nonlinear Saturation

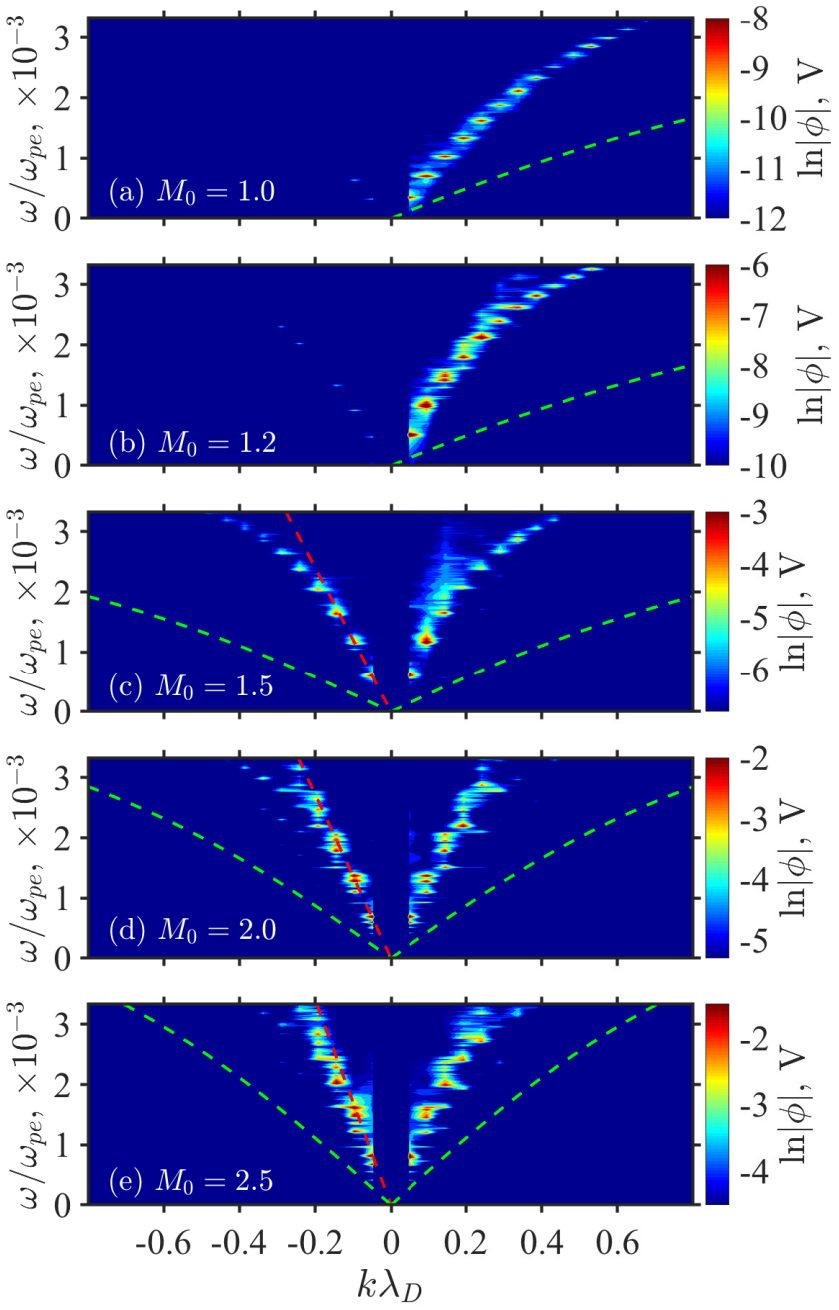

Figure 4.13: Dispersion diagrams for (a) $M_0 = 1.0$, (b) $M_0 = 1.2$, (c) $M_0 = 1.5$, (d) $M_0 = 2.0$, and (e) $M_0 = 2.5$. Domain length $L_1 = 130\lambda_D$. Red dashed lines for $M_0 = 1.5$, 2.0, and 2.5 show the approximate maximum phase velocity of the backward-propagating waves. Green dashed lines show phase velocity calculated from the warm ion acoustic speed $c_{s,\text{warm}}$ given by equation 4.9. Horizontal axes are in $k\lambda_D$, horizontal axes are in ω/ω_{pe}, and the contour color scale is in $\ln|\phi|$.

phase velocity. This is characteristic of the Buneman instability at large M_0 which is known for long-wavelength modes. The red dashed lines for $M_0 = 1.5$, 2.0, and 2.5 show the approximate maximum phase velocity of the backward-propagating ion acoustic waves that extend the ion VDFs to high negative velocities as shown in Figure 4.8. The green dashed lines show the warm ion acoustic speed $c_{s,\mathrm{warm}}$ which are observed to be much lower than the phase velocities from the simulation. For $M_0 = 2.0$ in Figure 4.13(d), the slope of the red dashed line was taken directly from the approximate maximum negative phase velocity observed from the backward-propagating waves in Figure 4.11(b), that is, $v_\phi = -8{,}066$ m/s, and one can see excellent agreement for the maximum negative phase velocity between the two figures. Fitting dashed red lines additionally to Figures 4.13(c) and 4.13(e), we get $v_\phi \approx -7{,}112$ m/s for $M_0 \approx 1.5$ and $v_\phi = -10{,}076$ m/s for $M_0 = 2.5$, respectively. We can compare this v_ϕ to the phase velocity for an ion solitary wave that satisfies the Korteweg-de Vries equation [53], given as $|v_\phi| = (1+\delta)c_{s,\mathrm{warm}}$ where $\delta = |\phi|_{\max}/3T_e$. If we solve for $\delta = |v_\phi|/c_{s,\mathrm{warm}} - 1$ using the $M_0 = 2.0$ simulation values for v_ϕ and $c_{s,\mathrm{warm}}$, we get $\delta \approx 0.70$. If we solve for $\delta = |\phi|_{\max}/3T_e$ using the simulation values for $|\phi|_{\max}$ and T_e, we get $\delta \approx 0.33$. Further, if we consider the maximum potential amplitude during long-time saturation for $M_0 = 2.0$ where $|\phi|_{\max} \approx 8$ V and $T_e \approx 8$ eV, the ion solitary wave speed is $|v_\phi| \approx 6{,}202$ m/s, compared to 8,066 m/s from the simulation. The KdV equation is derived from the fluid theory and neglects kinetic effects, so a cause of these discrepancies could be the electron and ion kinetic effects on the ion solitary waves.

The approximate maximum phase velocities for the backward-propagating ion acoustic waves were determined for the rest of the M_0 values for the cases $1.3 \geq M_0 \geq 2.5$ in the same way as the values for $M_0 = 1.5$, 2.0, and 2.5 were determined, and are shown as a function of M_0 in Figure 4.14. A 3rd-order polynomial was fitted to the simulation data as

$$|v_\phi^-|_{\max} = -1.1484 + 12.704M_0 - 7.1011M_0^2 + 1.5284M_0^3, \tag{4.10}$$

where $|v_\phi^-|_{\max}$ is in units of km/s. These data can be used along with knowledge of $|\phi|_{\max}$ to

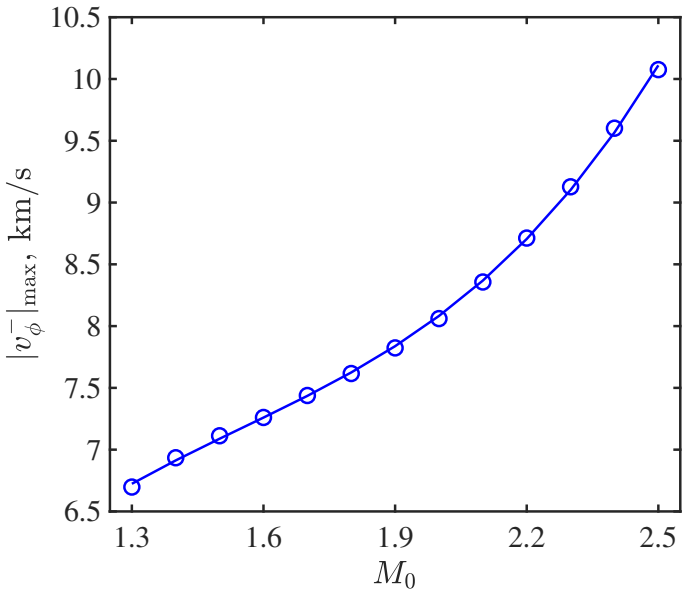

Figure 4.14: Simulation values for the magnitude of the approximate maximum negative phase velocity of the backward-propagating ion acoustic waves during nonlinear saturation for $1.3 \geq M_0 \geq 2.5$.

estimate the maximum energies that ions will obtain for a given M_0.

4.3.1 Ion Energy Distribution

The normalized ion energy distribution functions (EDFs) for argon and xenon were calculated for the backward-propagating ions in the spatio-temporally averaged VDFs in Fig. 4.8 using

$$E_i = \frac{1}{2}\frac{m_i}{e}v_{\text{neg}}^2, \tag{4.11}$$

where v_{neg} is the entire negative velocity range. The cases for $M_0 = 1.5$, 2.0, and 2.5 for argon and xenon ions are shown in Figure 4.15, and one can see that the ion EDFs have little to no dependence on the ion mass. This is expected due to the independence of the saturation electrostatic potential energy from ion mass as shown in Fig. 4.9.

With the Vlasov equation neglecting close-range collisions between particles, the energies obtained by the ions in these simulations are the result of collective interactions between particles

Backstreaming Ion EDFs during Nonlinear Saturation (reprinted from Ref. [44] with permission)

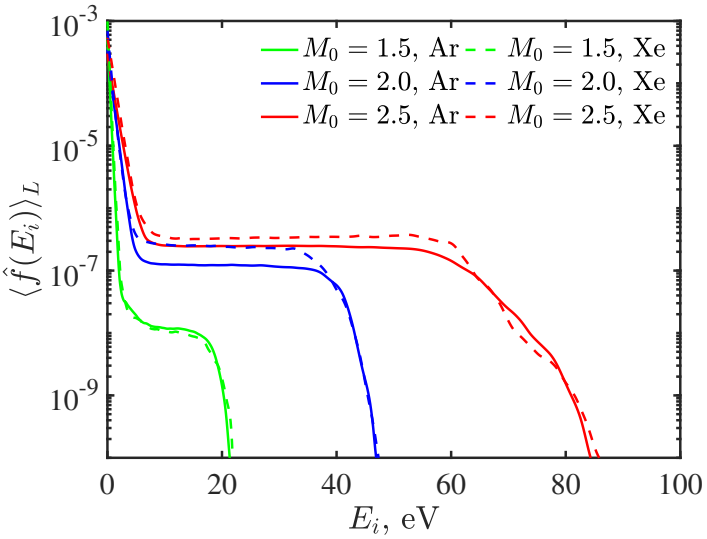

Figure 4.15: Normalized argon (40 amu) and xenon (131 amu) ion energy distribution functions for $M_0 = 1.5$, 2.0, and 2.5 calculated from the backward-propagating ions in the spatio-temporally averaged VDFs in Fig. 4.8. Reproduced from page 9 of Ref. [44]. First published May 21, 2019.

and plasma waves whose strength is determined by local deviations from quasineutrality. The maximum energy ions can obtain can be calculated from

$$E_{i,\max} = |\phi|_{\max} + \frac{1}{2}\frac{m_i}{e}(|v_\phi^-|_{\max} + \Delta v_{tr})^2, \tag{4.12}$$

where $\Delta v_{tr} = 2v_{th,i}\sqrt{|\phi|_{\max}/T_i}$ is the half-width of the trapped distribution centered around v_ϕ. Considering again the $M_0 = 2.0$ case, we have $|\phi|_{\max} \approx 8$ V, $|v_\phi^-|_{\max} \approx 8{,}066$ m/s, and $T_i \approx 0.35$ eV from the simulation results. If we use the initial ion temperature of $T_{i,0} = 0.2$ eV for the ion thermal velocity, $v_{th,i} = 694.2$ m/s. Substituting these values into the equation for $E_{i,\max}$, we get $E_{i,\max} \approx 53$ eV. This calculation has close agreement with the maximum energies of ions composing the plateau structure for $M_0 = 2.0$.

4.3.2 Ion Trapping Model

An algorithm was developed to extract the trapped ion populations from the 1D ion VDFs. The algorithm calculates the concavity of the ion VDF by taking $\partial^2 \hat{f}_i(v_i)/\partial v_i^2$ and approximating the bounds of the trapping regions by identifying the locations in velocity space where the concavity is at a maximum. The population of trapped ions can then be approximated by integrating $\hat{f}_i$ between these bounds. The goal here is to capture only the tails in the ion VDF and ignore the bulk ion population which do not have sufficient energies to overcome the threshold energy of material sputtering. This method works well for the tails in the ion VDF that form "plateau" structures, but is less accurate if the tails in the ion VDF are shaped more like an "elbow," such as what occurs for the ions trapped in the positive velocity for $M_0 = 1.2$ in Figure 4.8. The results of this algorithm operating on the full ion VDFs for $1.3 \leq M_0 \leq 2.5$, such as those shown in Figures 4.8(c2)-(e2), are shown in Figure 4.16. Neglected are the results for $M_0 \leq 1.2$ because our interest is in the possibility of material sputtering caused by the ions trapped in the plasma waves propagating with negative velocity.

The fraction of trapped ions $n_{tr,i}/n_i$ in plasma waves propagating with positive velocity and with negative velocity are shown in Figure 4.16(a). One can see that the population of ions trapped in forward-propagating plasma waves is consistently larger than that for backward-propagating plasma waves, though for $M_0 \geq 1.4$ the values are similar in order of magnitude. Shown in Figures 4.16(b) and (c) are the bounds of the forward and backward trapping regions that allowed for the calculation of $n_{tr,i}$, where $v_{\min}^{+}$ and $v_{\max}^{+}$ designate the bounds of ion trapping in the forward-propagating waves and $v_{\min}^{-}$ and $v_{\max}^{-}$ designate the bounds of ion trapping in the backward-propagating waves. These values are normalized by the initial cold ion sound speed $c_s = \sqrt{eT_{e,0}/m_i}$ to show deviation from particle trapping around the cold ion phase velocity. It can be seen in Figures 4.16(b) and 4.16(c) that ion trapping in both forward- and backward-propagating waves occurs over the same range of ion velocities, suggesting that the phase velocities of both the forward- and backward-propagating waves are equivalent as $\pm v_\phi$, which agrees with the observed phase velocities in Figures 4.11(b) and 4.11(e).

Ion Trapping Information (reprinted from Ref. [44] with permission)

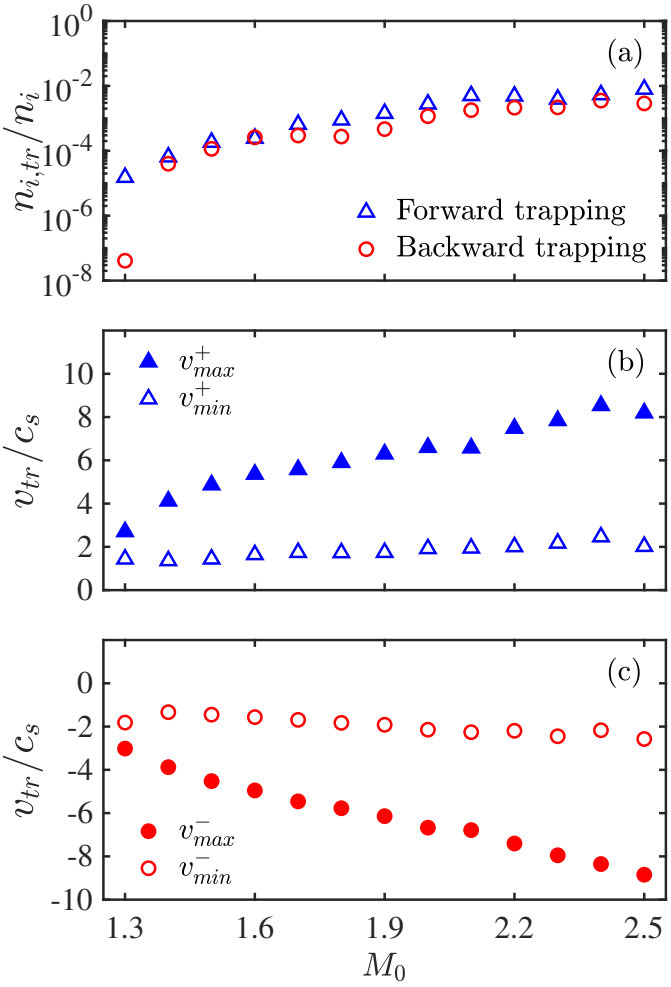

Figure 4.16: The high-energy tail of ion VDFs is extracted from the full ion VDFs shown in Fig. 4.8. (a) The fraction of the ion population that is trapped, $n_{i,tr}/n_i$, and (b) and (c) minimum and maximum velocities of the trapped ions, $v_{min}^{\pm}$ and $v_{\max}^{\pm}$, where superscript $\pm$ denotes the positive $(+)$ and negative $(-)$ velocity populations. The results are shown where negative velocity ion populations exist for $M_0 \geq 1.3$. Reproduced from page 9 of Ref. [44]. First published May 21, 2019. © IOP Publishing. Reproduced with permission. All rights reserved.

4.3.3 Material Sputtering

We have shown in Figure 4.11 that the current-driven instability at high M_0 can excite plasma waves propagating in the direction opposite to the exciting electron bulk velocity, and we have shown in Figures 4.5 and 4.8(b) that ions can be trapped in these backward-propagating waves leading to the growth of significant tails in the ion VDFs. Here, we will show that these back-

streaming ion populations can produce sputtering rates comparable to those measured in hollow cathode sputtering experiments.

The normalized sputtering rate $\hat{\Gamma}_{\mathrm{S,i}}$ of a material surface bombarded by backstreaming high-energy ions can be calculated as [54],

$$\hat{\Gamma}_{\mathrm{S,i}} = m_{target} \int Y(E_i)\hat{f}(v_i - u_i)v_i dv_i, \tag{4.13}$$

where m_{target} is the mass of the target surface material species, $Y(E_i)$ is the sputtering yield, $E_i = \frac{1}{2}m_i v_i^2/e$ is the ion energy in eV, and $u_i \leq 0$ is a possible ion drift velocity towards the material surface. Here, the target surface material is chosen to be molybdenum because it is commonly used for cathode orifice plates. Inclusion of the ion drift is to allow for comparison of the sputtering rate if there is an additional ion acceleration toward the cathode surface due to plasma and sheath potentials. For example, the energy gain by ions traveling through a sheath potential ϕ_w for a floating wall without secondary electron emission from the material can be calculated from $\phi_w = -T_e \ln\left(\sqrt{2\pi m_e/m_i}\right)$ [1, 55]. For $T_e = 0.5$ eV in an argon plasma, $\phi_w = 2.4$ V, which means the ions will pick up an additional 2.4 eV of energy.

Equation (4.13) can be used to calculate the normalized sputtering rate from the full ion VDFs shown in Figure 4.8(b) and for shifted Maxwellian ion VDFs with various u_i and T_i. Calculating the normalized sputtering rate for the ion trapping model discussed in the previous section involves integrating between the negative velocity trapping limits $v^-_{\max}$ and $v^-_{\min}$ in Figure 4.16(c) and using the values of $n_{i,tr}/n_i$ from Figure 4.16(a). Equation (4.13) is then modified as [44]

$$\hat{\Gamma}_{\mathrm{S,i}} = m_{target}\frac{n_{i,tr}}{n_i}\int_{v^-_{\min}+u_i}^{v^-_{\max}+u_i} Y(E_i)dv_{tr}. \tag{4.14}$$

The normalized sputtering rates calculated from the from the full ion VDFs using equation (4.13) and the ion trapping model using equation (4.14) are shown in Figure 4.17 as a function of M_0 and u_i for singly charged argon ions. The sputtering yield at normal incidence for argon was given by the model from Yamamura [56]. Although not shown, the sputtering rate for singly

Material Sputtering due to High Energy Ions (reprinted from Ref. [44] with permission)

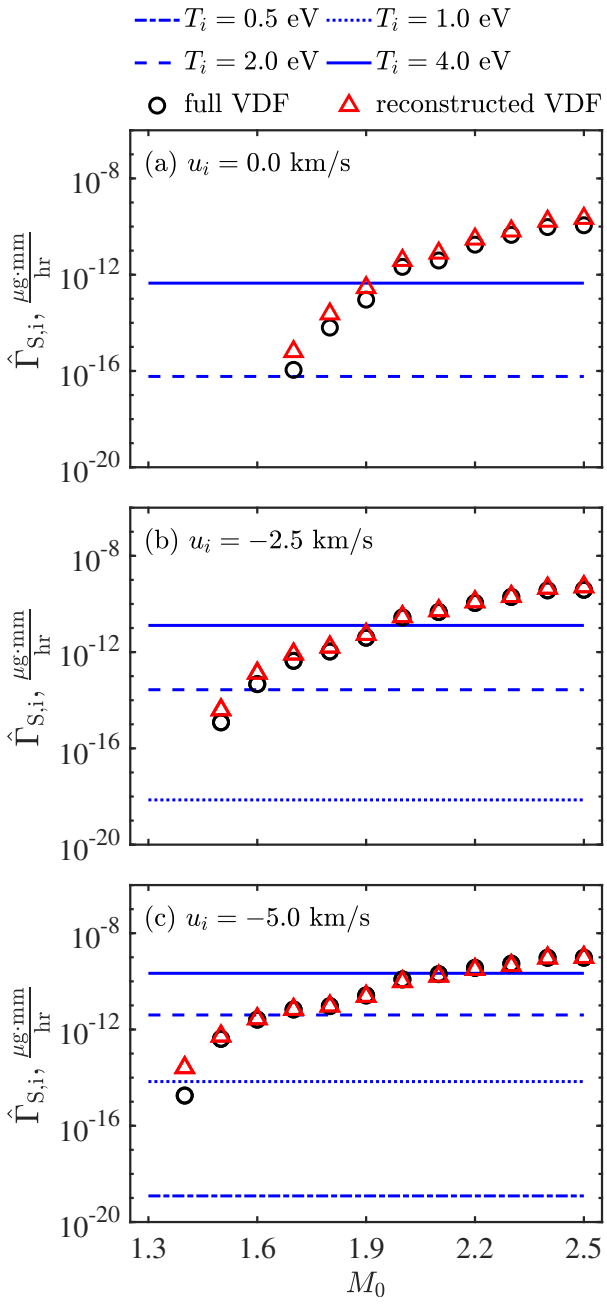

Figure 4.17: Sputtering rate as a function of initial electron Mach number, with sputtering yield calculated from the Yamamura model [56] for the argon case. Calculations using the ion VDFs obtained from the Vlasov simulations, as shown in Fig. 4.16, are compared to Maxwellians of varying temperatures and bulk velocity. Reproduced from page 10 of Ref. [44]. First published May 21, 2019.

charged xenon ions were calculated with a sputtering yield from Doerner et al. [57] and show good qualitative agreement with the calculations for singly charged argon. The Yamamura model is fitted to data for Ar^+ with Mo for incident energies of 40-10,000 eV, and is extrapolated for energies < 40 eV. The model by Doerner et al. is fitted to data for Xe^+ with Mo for incident energies of 10-200 eV, and thus is expected to produce a more accurate sputtering yield at lower incident ion energies than the Yamamura model, which is especially important for the ion energies observed in hollow cathode plumes [6]. It can be seen that the sputtering rates calculated from the ion trapping model yields good agreement with the sputtering rates calculated from the full ion VDFs for $M_0 \geq 1.5$. The reason for significant discrepancies for $M_0 < 1.5$ is due to the difficulty of the ion trapping model in accurately capturing the trapped ion populations when they do not form the neat "plateau" structures that can be observed for $M_0 \geq 1.5$. Figure 4.17(a) shows the sputtering rate calculated assuming an ion VDF with zero drift, while Figures 4.17(b) and (c) show the sputtering rate for ion VDFs with a drift velocity representing ion acceleration towards the cathode resulting from a potential drop near the surface, which can be caused by plasma and sheath potentials. For these cases, $u_i = -2.5$ km/s corresponds to an increase in ion energy of 1.3 eV and $u_i = -5$ km/s corresponds to an increase in ion energy of 5.2 eV. It can be seen that inclusion of the ion bulk velocity in the negative direction significantly increases the sputtering rate due to the larger population of backward-propagating ions that can contribute to sputtering.

Also shown in Figure 4.17 are the normalized sputtering rates calculated with Maxwellian ion VDFs with temperatures $0.5 \leq T_i \leq 4$ eV. It can be seen by comparing these sputtering rates to those calculated from the kinetic simulations that relatively high ion temperatures are necessary in a fluid model for calculating sputtering rates comparable to what can occur for kinetic ions resulting from a high M_0 current-driven instability, with ion temperatures up to 4 eV needed as M_0 increases to 2.5.

The mass loss rate per unit area of the surface material can be calculated as $\dot{m}_{\text{loss}} = n_{\text{plasma}}\hat{\Gamma}_{\text{S,i}}$, where n_{plasma} is the number density of the plasma wave. This mass loss rate calculated from the simulations can then be compared to mass loss rate data obtained experiments. Kolasinski

et al. [58] reported mass loss rates per unit area on the order of $0.1 - 0.8$ μg/(mm^2-hr) for an NSTAR configuration ion engine hollow cathode using xenon propellant. Assuming the plasma density where the high energy ions are generated is $n_{\mathrm{plasma}} = 10^9$ mm^{-3} and an ion drift velocity of $u_i = -5$ km/s, the required normalized sputtering rate would be $\hat{\Gamma}_{\mathrm{S,i}} \approx 10^{-10}$ μg-mm/hr. It can be seen from Figure 4.17(c) that achieving that level of sputtering with a fluid model would require $T_i = 4$ eV. It can also been from Figure 4.17(c) that approximately the same level of sputtering is caused by the kinetic ions from the simulation with $M_0 = 2$ and $T_{i,0} = 0.2$ eV. Further, Maxwellian ion temperatures exceeding 2 eV in the hollow cathode plume can be considered unreasonable as fluid models that account for ion heating due to the saturated plasma waves would likely suffer from effects of coupling these high ion temperatures with the rest of the system, such as ion Landau over-damping the instability due to the excessively high ion temperatures. Recent numerical simulations by Jorns et al. calculate ion temperatures of up to 2 eV along the cathode centerline using data from experimental measurements [23], and Ortega et al. found a maximum $T_i \approx 2$ eV in their 2-D hydrodynamic simulations, which account for the growth and saturation of the instability [13]. A coupled plasma-thermal model by Sary et al. showed ion temperatures up to 3,000 K [11].

5. SUMMARY AND FUTURE WORK

5.1 Summary

A 1D Vlasov-Poisson simulation is used to study collisionless current-driven instabilities for initial conditions of $T_{e,0}/T_{i,0} = 10$ and $0.5 \leq M_0 \leq 2.5$. The dominant modes during linear growth are shown to occur at larger wavelengths as M_0 increases, and the growth rate for $M_0 = 0.5$ agrees with the linear theory. Large amplitude potential oscillations occur during nonlinear saturation and are shown to scale rapidly with increasing M_0 and the electrostatic potential energies during nonlinear saturation are shown not to scale with ion mass, however ion mass does reduce the growth rate as predicted by theory. The time evolution of the bulk plasma properties, such as the electron Mach number, electron temperature, and ion temperature is shown in the range of $1.0 \leq M_0 \leq 2.5$ and it is shown that the plasma is effectively heated as energy is drawn from the exciting electron current, resulting in a decrease in the electron Mach number over time, and this decrease is more significant as the initial condition M_0 increases. This shows that the bulk plasma is significantly affected by the instability, and because the instability grows rapidly, experimental measurements cannot be used to predict the growth rate. Various effective collision frequency models are discussed and compared and it is found that the wave growth model derived in Ref. [13] and the model derived from Ohm's Law with a dependence on the electrostatic potential energy share a good qualitative agreement.

Ion velocity distribution functions are shown along with potential fluctuation amplitudes and a significant population of backstreaming high energy ions is observed when the initial electron Mach number is greater than or equal to 1.3 due to the generation of large amplitude backward-propagating ion acoustic waves. It is shown that the potential amplitude oscillations due not depend on the ion mass. Maximum and root-mean-square potentials are shown fitted to functions of M_0, which can be used as inputs to Hall thruster boundary conditions in fluid models. The potential amplitudes as a function of wave number are shown with scaling fits and compared to theory.

Dispersion diagrams show the phase velocities of the waves and the increase of the maximum phase velocity with increasing M_0 is shown. Ion energy distribution functions are calculated from the velocities distribution functions and it is shown that the ion energies can extend out to 20-80 eV for $M_0 = 1.5$ to 2.5 and do not depend on ion mass.

A model that extracts the populations and velocity ranges of high energy ions is provided and used to calculate sputtering rates, which are compared to sputtering rates calculated using the non-Maxwellian ion VDFs obtained from the Vlasov simulation and Maxwellian distribution of varying ion temperatures and drift velocities. It is shown that the Maxwellian distributions require very large ion temperatures to predict the same sputtering rates as the kinetic ions.

5.2 Future Work

We can think about anomalous electron transport by considering the role of electron pressure

$$\frac{du_e}{dt} = -\frac{eE}{m_e} - \frac{1}{en_e}\frac{\partial p_{e,\text{Maxwellian}}}{\partial x} - \nu_m u_e,$$

where we have split the electron pressure p_e into a Maxwellian term and a non-Maxwellian term $p_e = p_{e,\text{Maxwellian}} + p_{e,\text{nonMaxwellian}}$. As shown in Figure 4.5, the anomalous resistivity corresponds to a highly non-Maxwellian electron VDF, such that essentially during steady state,

$$\frac{1}{en_e}\frac{\partial p_{e,\text{nonMaxwellian}}}{\partial x} = \nu_m u_e.$$

This will be investigated in future work.

Future kinetic simulation efforts will include higher dimensions with realistic boundary conditions and the effects of collisions on the growth of the instability. A study of the startup process of the hollow cathode and the growth of the instability during this early stage would be very informative as to determining the nature of the instability as it occurs in hollow cathode plumes during steady state operation. Incorporating nonlinear ion dynamics during the rapid growth process to current theories is necessary to accurately predict both the state of nonlinear saturation for M_0 and

the proper kinetic evolution of the ion velocity distribution, from which a new growth rate model and a model of the high energy ions for incorporation into fluid codes can be derived.

REFERENCES

[1] Goebel D and Katz I 2008 *Fundamentals of Electric Propulsion: Ion and Hall Thrusters* (Wiley)

[2] Goebel D M, Watkins R M, Jameson K K 2007 *J. Propul. Power* **23** 552–558

[3] Mikellides I G, Katz I, Goebel D M and Jameson K K 2007 *J. Appl. Phys* **101** 063301

[4] Mikellides I G, Katz I, Goebel D M and Polk J E 2005 *J. Appl. Phys* **98** 113303

[5] Jorns B, Goebel D M and Mikellides I G 2014 Investigation of Energetic Ions in a 100-A Hollow Cathode *50th AIAA/ASME/SAE/ASEE Joint Propulsion Conference* (Cleveland, OH: AIAA paper 2014-3826)

[6] Goebel D M, Jameson K K, Katz I and Mikellides I G 2007 *Phys. Plasmas* **14** 103508

[7] Mikellides I G, Katz I, Goebel D M, Jameson K K and Polk J E 2008 *J. Propul. Power* **24** 866–879

[8] Mikellides I G, Katz Ira, Goebel D M and Polk J E 2008 Assessments of Hollow Cathode Wear in the Xenon Ion propulsion System (XIPS) by Numerical Analysis and Wear Tests *44th AIAA/SAE/ASEE Joint Propulsion Conference* (Hartford, CT: AIAA paper 2008-5208)

[9] Ong R S B and Yu M Y 1969 *J. Plasma Phys* **3** 425–433

[10] Epperlein E M, Short R W and Simon A 1992 *Phys. Rev. Lett* **69** 1765–1768

[11] Sary G, Garrigues L and Boeuf J P 2017 *Plasma Sources Sci. Technol* **26** 055007

[12] Sary G, Garrigues L and Boeuf J P 2017 *Plasma Sources Sci. Technol* **26** 055008

[13] Ortega A L, Jorns B and Mikellides I G 2018 *J. Propul. Power* **34** 1026–1038

[14] Banks J W, Berger R L, Brunner S, Cohen B I, and Hittinger J A F 2011 *Phys. Plasmas* **18** 052102

[15] Stringer T E 1964 *J. Nucl. Energy, Part C* **6** 267–279

[16] Lampe M, Manheimer W M, Mcbride J B and Orens J H 1972 *Phys. Fluids* **15** 2356–2362

[17] Davidson R C and Krall N A 1977 *Nucl. Fusion* **17** 1313–1372 5ISSN 17414326

[18] Omura Y, Heikkila W J, Umeda T, Ninomiya K and Matsumoto H 2003 *J. Geophys. Res: Space Physics* **108** 1197

[19] Tokluoglu E K, Kaganovich I D, Carlsson J A, Hara K and Startsev E A 2018 *Phys. Plasmas* **25** 052122

[20] Hara K, Kaganovich I D and Startsev E A 2018 *Phys. Plasmas* **25** 011609

[21] Berman R H, Tetreault D J, Dupree T H and Boutros-Ghali T 1982 *Phys. Rev. Lett* **48**(18) 1249–1252

[22] Lesur M, Diamond P H and Kosuga Y 2014 *Plasma Phys. Control. Fusion* **56** 075005

[23] Jorns B A, Dodson C, Goebel D M and Wirz R 2017 *Phys. Rev. E* **96**(2) 023208

[24] Hara K and Hanquist K M 2018 *Plasma Sources Sci. Technol* **27** 065004

[25] Jorns B A, Lopez-ortega A and Mikellides I G 2016 First-principles Modelling of the IAT-driven Anomalous Resistivity in Hollow Cathode Discharges I : Theory *52nd AIAA/SAE/ASEE Joint Propulsion Conference* (Salt Lake City, UT: AIAA paper 2016-4626)

[26] Lopez Ortega A, Mikellides I G and Jorns B 2016 First-principles modeling of the IAT-driven anomalous resistivity in hollow cathode discharges II: Numerical simulations and comparison with measurements *52nd AIAA/SAE/ASEE Joint Propulsion Conference* (Salt Lake City, UT: AIAA paper 2016-4627)

[27] Kubota K, Oshio Y, Watanabe H, Cho S and Funaki I 2018 Numerical Simulation of Hollow Cathode with Hybrid-PIC Coupled with Growth Model of Ion Acoustic Turbulence *2018 Joint Propulsion Conference* (Cincinnati, OH: AIAA paper 2018-4513)

[28] Harris S 2004 *An Introduction to the Theory of the Boltzmann Equation* (Dover)

[29] Grad H 1949 *On the kinetic theory of rarefied gases*

[30] Fitzpatrick R 2014 *Plasma Physics: An Introduction* (Taylor & Francis)

[31] Fried B D and Conte S D 1961 *The plasma dispersion function* (N.Y. : Academic Press)

[32] Buneman O 1958 *Phys. Rev. Lett* **1** 8–9

[33] Buneman O 1959 *Phys. Rev.* **115** 503–517

[34] Bartlett C J 1968 *Phys. Fluids* **11** 822

[35] Ishihara O, Hirose A and Langdon A B 1981 *Phys. Fluids* **24** 452–464

[36] Hirose A, Ishihara I, Langdon A B 1982 *Phys. Fluids* **25** 610

[37] Chapman T, Brunner S, Banks J W, Berger R L, Cohen B I and Williams E A 2014 *Phys. Plasmas* **21** 042107

[38] Berger R L, Brunner S, Chapman T, Divol L, Still C H and Valeo E J 2013 *Phys. Plasmas* **20** 032107

[39] Brunner S, Berger R L, Cohen B I, Hausammann L and Valeo E J 2014 *Phys. Plasmas* **21** 102104

[40] Ishihara O, Hirose A 1981 *Phys. Rev. Lett* **46**(12) 771–774

[41] Hizanidis K, Kominis Y, Ram A K 2010 *Plasma Phys. Control. Fusion* **52** 124022

[42] Bychenkov V Y, Silin V P and Uryupin S A 1988 *Phys. Rep* **164** 119–215

[43] Hara K 2015 *Development of Grid-Based Direct Kinetic Method and Hybrid Kinetic-Continuum Modeling Modeling of Hall Thruster Discharge Plasmas* Ph.D. thesis University of Michigan

[44] Hara K, Treece C 2019 *Plasma Sources Sci. Technol.* **28** 055013 DOI: https://doi.org/10.1088/1361-6595/ab18e4

[45] Goebel D M, Jameson K, Katz I, Mikellides I G 2005 Energetic Ion Production and Electrode Erosion in Hollow Cathode Discharges *29th International Electric Propulsion Conference* (Princeton University: IEPC paper 2005-266)

[46] Sagdeev R Z and Galeev A A 1966 *Lectures on the nonlinear theory of plasma* (Piazza Oberdan)

[47] Lopez Ortega A and Mikellides I G 2016 *Phys. Plasmas* **23** 043515

[48] Boyd I D and Dressler R A 2002 *J. Appl. Phys* **92** 1764–1774

[49] Mikellides I G, Katz Ira, Hofer R R and Goebel D M 2009 Hall-Effect Thruster Simulations with 2-D Electron Transport and Hydrodynamic Ions *Proceedings of the 31st International Electric Propulsion Conference* (Ann Arbor, MI: IEPC paper 2009-114)

[50] Fife J M 1998 *Hybrid-PIC Modeling and Electrostatic Probe Survey of Hall Thrusters* Ph.D. thesis MIT

[51] Parra F I, Ahedo E, Fife J M and Martínez-Sánchez M 2006 *J. Appl. Phys* **100** 023304

[52] Boeuf J P 2017 *J. Appl. Phys* **121** 011101

[53] Chen F 2016 *Introduction to Plasma Physics and Controlled Fusion* (Springer)

[54] Domonkos M T, Foster J E, Patterson M J and George J Williams J 2001 Investigation of Keeper Erosion in the NSTAR Ion Thruster *27th International Electric Propulsion Conference* (Cleveland, OH: IEPC-01-308)

[55] Barral S, Makowski K, Peradzynski Z, Gascon N and Dudeck M 2003 *Phys. Plasmas* **10** 4137–4152

[56] Yamamura Y and Tawara H 1996 *At. Data Nucl. Data Tables* **62** 149–253

[57] Doerner R P, Whyte D G and Goebel D M 2003 *J. Appl. Phys* **93** 5816

[58] Kolasinski R D and Polk J E 2004 *J. Propul. Power* **20** 992–999